Dalton Transactions

PAPER

View Article Online
View Journal | View Issue

Cite this: *Dalton Trans.*, 2025, **54**, 12358

Synthesis, characterization, crystal structure and comparative study of porous metal–organic frameworks, ternary quantum dots and their composite as sensors for the electrochemical determination of bisphenol A†

Peter A. Ajibade * and Solomon O. Oloyede

Received 16th February 2025,
Accepted 3rd July 2025

DOI: 10.1039/d5dt00377f

rsc.li/dalton

Sensitive and rapid electrochemical sensors for bisphenol A (BPA) determination were developed using metal–organic frameworks (MOFs), ternary quantum dots (TQDs), and their composite (TQDs@MOFs). The electrochemical sensors were characterized using FTIR, UV-Vis, SEM, TEM, PL, and single X-ray crystallography. Electrochemical responses using cyclic voltammetry (CV) and differential pulse voltammetry (DPV) reveal that the composite modified electrode has an enhanced response and performed better and faster with the highest oxidation peak current of 2.70×10^{-4} over a suitable potential separation window of 0.939 V. Under optimized conditions and over an examined concentration range from 4 ηM to 16 ηM, the composite modified electrode displays a linear relationship with an increase in concentration with a limit of detection of 1.01 ηM, a limit of quantitation of 3.08 ηM, and a correlation coefficient (R^2) of 0.995 (S/N = 3). The composite modified electrode demonstrated good stability, reproducibility, and selectivity in the presence of other interfering substances. The practicability of the composite modified electrode was achieved using real water samples with a percentage recovery of 96.46–101.70% and a relative standard deviation of 3.22–5.06%.

1. Introduction

Endocrine disruptors (EDs) are chemicals that interfere with endocrine (or hormonal) systems,[1] but they are also occasionally referred to as hormonally active agents (HAAs), endocrine disrupting chemicals (EDCs), or endocrine disrupting substances (EDSs).[2–4] Endocrine disrupting chemicals cause changes in the normal functioning of the endocrine systems which leads to other diseases in humans.[5–8] Endocrine disruptors are present in a wide range of consumer and industrial products and their exposure interferes with the synthesis, secretion, transport, binding, action, or elimination of natural hormones in the body that are responsible for development, behaviour, fertility, and normal cell metabolism.[9–13]

Bisphenol A (BPA) [2,2-bis(4-hydroxyphenyl)propane] is one of the most dangerous EDCs that is primarily employed in the production of different plastics.[14–18] Food is the main source of exposure for humans since food cans are lined with PVC and epoxy to stop acidic foods from corroding the metal.[19–21] Once in the human biological system, BPA may imitate the hormone oestrogen in the body, leading to endocrine disorders, prostate cancers, and developmental delays in children, among other diseases. In response to this side effect, it is therefore important to develop new detection and determination methods with high selectivity and high efficiency to facilitate regular monitoring of BPA levels in the environment.[22–24]

Numerous techniques have been developed to determine BPA such as electrophoresis,[25–27] enzyme linked immunosorbent assay,[28,29] gas chromatography-mass spectrophotometry,[30–32] high-pressure liquid chromatography,[33–35] fluorescence spectrometry,[36] liquid-chromatography-mass spectrometry,[37] and gas chromatography.[38–40] These techniques require expensive equipment and trained specialists. Therefore, the development of a simple, fast, low-cost detection method is necessary. Electrochemical techniques for highly sensitive, highly selective, rapid, low-cost, and real-time detection of BPA with ease of automation are being developed.[41] Yet, because of its relatively high potential for the oxidation of phenolic compounds, which causes an increase in background current and a loss in sensitivity, direct detection of BPA using a standard bare gold electrochemical electrode is still limited.[42,43] There have been several modifications of

---

School of Chemistry and Physics, University of Kwazulu-Natal, Private Bag X01, Pietermaritzburg 3209, South Africa. E-mail: ajibadep@ukzn.ac.za

† Electronic supplementary information (ESI) available. CCDC 2254565. For ESI and crystallographic data in CIF or other electronic format see DOI: **https://doi.org/10.1039/d5dt00377f**

the electrodes to detect BPA in order to improve the sensitivity and selectivity of the detection process. These include gold nanoparticles,[44] multiwalled carbon nanotubes,[45] thionine-tyrosinase,[46] graphene,[47] and graphene oxide–β-cyclodextrin multiwalled carbon nanotubes.[48]

In recent years, metal–organic frameworks (MOFs) have demonstrated considerable potential as sensors for the detection of metal ions, organic dyes, and environmental pollutants. As a result of MOFs' unparalleled structural flexibility,[49] tunable topology,[50] various functionality, large surface area, adjustable spectrum and porosity,[51] a variety of nanomaterials may be embedded into the pores of MOFs, which endows them with the ability to be used in different applications such as gas adsorption and separation,[52] chemical sensors,[53] catalysis,[54] magnetic and luminescent materials,[55] biomedical imaging,[56] drug loading and delivery,[57] absorption,[58] *etc*. The reaction of these porous compounds with a wide range of environmental pollutants and the ability of the compounds to detect them are also enhanced due to the synergistic interactions between the embedded nanomaterials, the functionality of the ligands, and the nature of the cluster. MOFs can increase sensor sensitivity by pre-concentrating the analyte (BPA) through hydrogen bonding and π–π interactions. In the synthesis of MOFs, it may be feasible to choose metal ions and organic linkers to promote specific responses with the analyte. The sensing performance of MOFs is also enhanced by acting as scaffolds for binding ternary quantum dots, enzymes, and nanoparticles.[59]

Ternary quantum dots (TQDs) are among the most well-known luminous nanomaterials with enhanced biocompatibility, superior photostability, minimal cytotoxicity, enhanced optical properties, and concentrated energy emission. Ternary quantum dots are useful for chemical sensing,[52] biosensing,[53] photocatalysts,[54] cell imaging,[55] drug delivery,[56] and nanomedicines.[57] Ternary quantum dots exhibit strong fluorescence emission, which makes them more sensitive to quenching or amplification when interacting with the analyte. They have a high surface-to-volume ratio and low cytotoxicity, which makes it easier and more effective to monitor the analyte.[60] The benefits of the combination of MOFs and TQDs include better signal transduction in which MOFs maintain quantum efficiency by stabilising and dispersing TQDs, avoid aggregation, improve selectivity and sensitivity through which MOFs pre-filter interference and improve BPA specificity by acting as molecular sieves.[61]

In this paper, a gold bare electrode was modified using metal–organic frameworks (MOFs/AuE), ternary quantum dots (TQDs/AuE), and their conjugate (TQDs@MOFs/AuE) respectively for the electrochemical determination of BPA using cyclic voltammetry (CV) and differential pulse voltammetry (DPV). An electrochemical comparative study between the precursors and their composite was used to ascertain the high performance, efficiency and sensing abilities displayed by the conjugate modified gold electrode with respect to the metal–organic frameworks and ternary quantum dots, respectively.

2. Experimental

2.1. Chemicals and reagents

All chemicals and reagents were purchased from Sigma Aldrich and used without further purification. Copper(II) chloride dihydrate $(CuCl_2)\cdot 2H_2O$, 2-methyl imidazole, benzene 1,3,5-tricarboxylic acid, copper(II) chloride anhydrous $(CuCl_2)$, indium chloride $(InCl_3)$, gelatin, glutathione (GSH), sodium sulfide (NaS_2), dimethylformamide (DMF), thioglycolic acid, selenium standard solution in nitric acid ((SeO_2) in HNO_3), distilled water, deionized water, ultra-pure water, ethanol, triethylamine (TEA), bisphenol A (BPA), potassium ferricyanide $[K_3(Fe(CN)_6)]$, and potassium chloride (KCl).

2.2. Physical measurements

Transmission electron microscopy (TEM) images were obtained using a JEOL JEM-2100 electron microscope (Akishima, Tokyo, Japan). The surface morphology was determined by scanning electron microscopy (SEM) using a ZEISS FESEM Ultra Plus (Oberkochen, Germany) at a rating voltage of 15–20 kV at different magnifications as indicated on the SEM images. Fourier transform infrared spectra were recorded using a Bruker ALPHA II compact platinum ATR FTIR spectrometer, ultra-violet–visible (UV-Vis) spectra were recorded on a PerkinElmer Lambda 25 UV-Vis spectrophotometer using dimethylsulfoxide (DMSO) at room temperature and the photoluminescence (PL) study was performed with a PerkinElmer LS 45 fluorescence spectrometer excited at 500 nm using DMSO at room temperature. All electrochemical studies, including differential pulse voltammetry (DPV), cyclic voltammetry (CV), and electrochemical impedance spectroscopy (EIS), were carried out in an Autolab PGSTAT 302N electrochemical workstation containing an electrochemical impedance module (EIM). A standard three electrode system containing a gold or platinum working electrode, a Ag/AgCl wire as a pseudo reference electrode, and platinum (Pt) as a counter electrode was used for the electrochemical experiments at ambient temperature.

2.3. Synthesis of $[Cu_2(BTA)_2(2\text{-MeIm})_6]$ (MOF) compound 1

The synthesis method of Dewangan *et al.*[58] was adopted for the preparation of metal–organic frameworks with some modifications. Copper(II) chloride dihydrate $(CuCl_2)\cdot 2H_2O$ (1 mmol, 0.170 g) was dissolved in 10 mL of distilled water and stirred at room temperature for 15 min. 2-Methyl imidazole (2-MeIm) (6 mmol, 0.5 g) and benzene 1,3,5-tricarboxylic acid (BTA) (2 mmol, 0.420 g) were each dissolved in 10 mL of DMF and stirred at room temperature for 45 min. The two solutions of 2-MeIm and BTA were mixed, and a colourless solution was obtained, which was stirred at room temperature for another 20 min. This was followed by the addition of an aqueous solution of (1 mmol, 0.170 g) copper(II) chloride dihydrate $(CuCl_2\cdot 2H_2O)$. The resulting blue clear solution was then stirred at room temperature for 30 min and then refluxed for 6 h at 80 °C under nitrogen gas (inert atmosphere). The obtained clear blue solution was centrifuged at 5000 rpm (revolutions per minute), filtered to remove impurities and kept at room temperature for slow evaporation. Blue crystals suitable for single crystal X-ray analysis were harvested after 4 weeks. These blue crystals were washed with DMF and ethanol at a ratio of 1 : 1 and kept at room temperature in a desiccator for further characterization. Scheme 1 illustrates the graphical synthesis pathway, and Scheme 2 illustrates the chemical or laboratory synthesis pathway of compound **1**. % Yield: 83%; 1.0 g, M. pt = 398 °C. FTIR (ν_{max}/cm^{-1}), ν(O–H) 3027 cm^{-1}, ν(N–H) 3433 cm^{-1}, ν(C–H) 2880 cm^{-1}, ν(C=C) 1640 cm^{-1}, ν(C=O) 1685 cm^{-1}, ν(C–O) 1091 cm^{-1}, ν(Cu–O) 522 cm^{-1}, ν(Cu–N) 573 cm^{-1} UV-Vis (DMSO, λ_{max}) 222 nm, 438 nm, 499 nm, 549 nm, 628 nm. Analytical for $C_{42}H_{42}Cu_2N_{12}O_{12}$ calculated 1033.98 g mol^{-1}, C: 48.74; H: 4.06; N: 16.24; O: 18.57; Cu: 12.16. Found 1033.95 g mol^{-1} C: 47.75; H: 4.06; N: 16.25; O: 18.57; Cu: 12.28.

2.4. Molecular structure of compound 1

Single crystals suitable for X-ray crystallography of compound **1** were obtained by slow evaporation of the compound in DMF/water. Data collection was performed using a Bruker APEX-II CCD diffractometer with MoKα graphite-monochromated single radiation (λ = 0.71073), and the crystals were maintained at 1002.02 K during the collection. Using Olex2,[62] the structure was resolved with the SHELXT[63] structure solution program using intrinsic phasing and refined with the SHELXL[64] refinement package using least squares minimization.

2.5. Synthesis of TQD ($CuInS_2$) compound 2

The method of Muñoz *et al.*[65] was adopted with some modifications. $CuCl_2$ (2 mmol, 0.340 g) and $InCl_3$ (2 mmol, 0.442 g) were both dissolved in 20 mL of deionized water. Gelatin (8 mmol, 1.44 g), sodium citrate (4 mmol, 1.176 g), thioglycolic acid (8 mmol, 0.736 g), and sodium sulfide hydrate (Na_2S) (4 mmol, 0.312 g) were all dissolved in 80 mL of deionized water and the solution was added to the previous 20 mL solution of $CuCl_2$ and $InCl_3$. Sodium borohydride ($NaBH_4$) (8 mmol, 0.3055 g) in 15 mL of distilled water was then added to the mixture above for the reduction of toxicity and stabilisation of ternary quantum dots. The whole mixture was then refluxed at 180 °C for 4 h under nitrogen gas, and the final product was centrifuged at 5000 rpm, filtered, and washed three times with deionized water to obtain $CuInS_2$ ternary core quantum dots. The product was kept in a desiccator for further characterization. Yield 85%, 4.038 g, M. pt = 265 °C. FTIR (ν_{max}/cm^{-1}), ν(C–S) 479 cm^{-1}, ν(C=O) 1789 cm^{-1}, ν(C–O) 1100 cm^{-1}, ν(O–H) 3009 cm^{-1}, ν(N–H) 3829 cm^{-1} ν(C–H) 2950 cm^{-1}, ν(Cu–In) 615 cm^{-1}, ν(S–H) 2712 cm^{-1}, ν(C–N) 998 cm^{-1}, ν(C–C) 1345 cm^{-1}, UV-Vis (DMSO, λ_{max}) 265 nm, 524 nm, 588 nm.

2.6. Synthesis of composite [TQDs@MOFs] [$CuInS_2$@Cu(2-MeIm)$_6$(BTA)$_2$] compound 3

The synthesis method of Alsaiari *et al.* was employed to prepare compound **3** with some modifications.[66] $CuCl_2$ (1 mmol, 0.170 g) and $InCl_3$ (1 mmol, 0.221 g) were dissolved in 10 mL of deionized water. Gelatin (4 mmol, 0.72 g), sodium citrate (2 mmol, 0.588 g), thioglycolic acid (4 mmol, 0.368 g), and sodium sulfide hydrate (Na_2S) (2 mmol, 0.156 g) were all dissolved in 40 mL of deionized water. Sodium borohydride ($NaBH_4$) (4 mmol, 0.1527 g) in 5 mL of distilled water was then added for the reduction of toxicity and stabilisation of ternary quantum dots. The whole mixture was stirred for 15 min and then refluxed for 1 h and 30 min at 85 °C. A known mass of 0.8 g of metal–organic frameworks was then added to the above mixture and the reflux was continued for another 2 h under nitrogen gas. After this, the resulting composite [$CuInS_2$@Cu(2-MeIm)$_6$(BTA)$_2$] was precipitated by adding 3 mL of ethanol, centrifuged at 5000 rpm and filtered. The composite was washed with DMF and ethanol at a ratio of 1 : 1, dried and kept in a desiccator. Scheme 3 depicts the graphical synthesis pathway for compound **3**. % Yield 94%, 2.97 g, M. pt 365 °C. FTIR (ν_{max}/cm^{-1}), ν(O–H) 3027 cm^{-1}, ν(N–H) 3433 cm^{-1}, ν(C–H) 2880 cm^{-1}, ν(C=C) 1640 cm^{-1}, ν(C=O) 1685 cm^{-1}, ν(C–O) 1091 cm^{-1}, ν(Cu–O) 522 cm^{-1}, ν(C–S) 479, ν(Cu–In) 615 cm^{-1}, ν(S–H) 2712 cm^{-1}, ν(Cu–N) 998 cm^{-1}. UV-Vis (DMSO, λ_{max}) 267 nm, 386 nm, 396 nm, 300 nm.

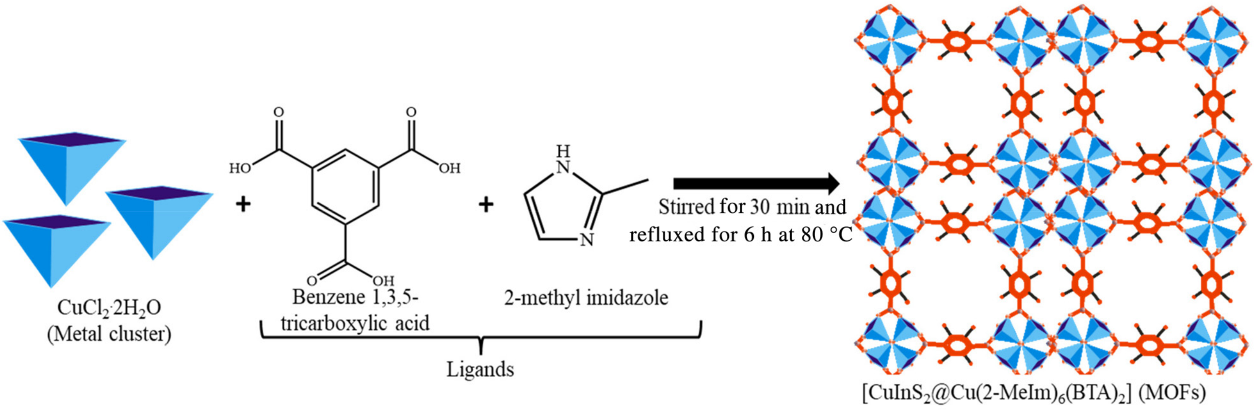

Scheme 1 Graphical synthesis pathway of compound **1**.

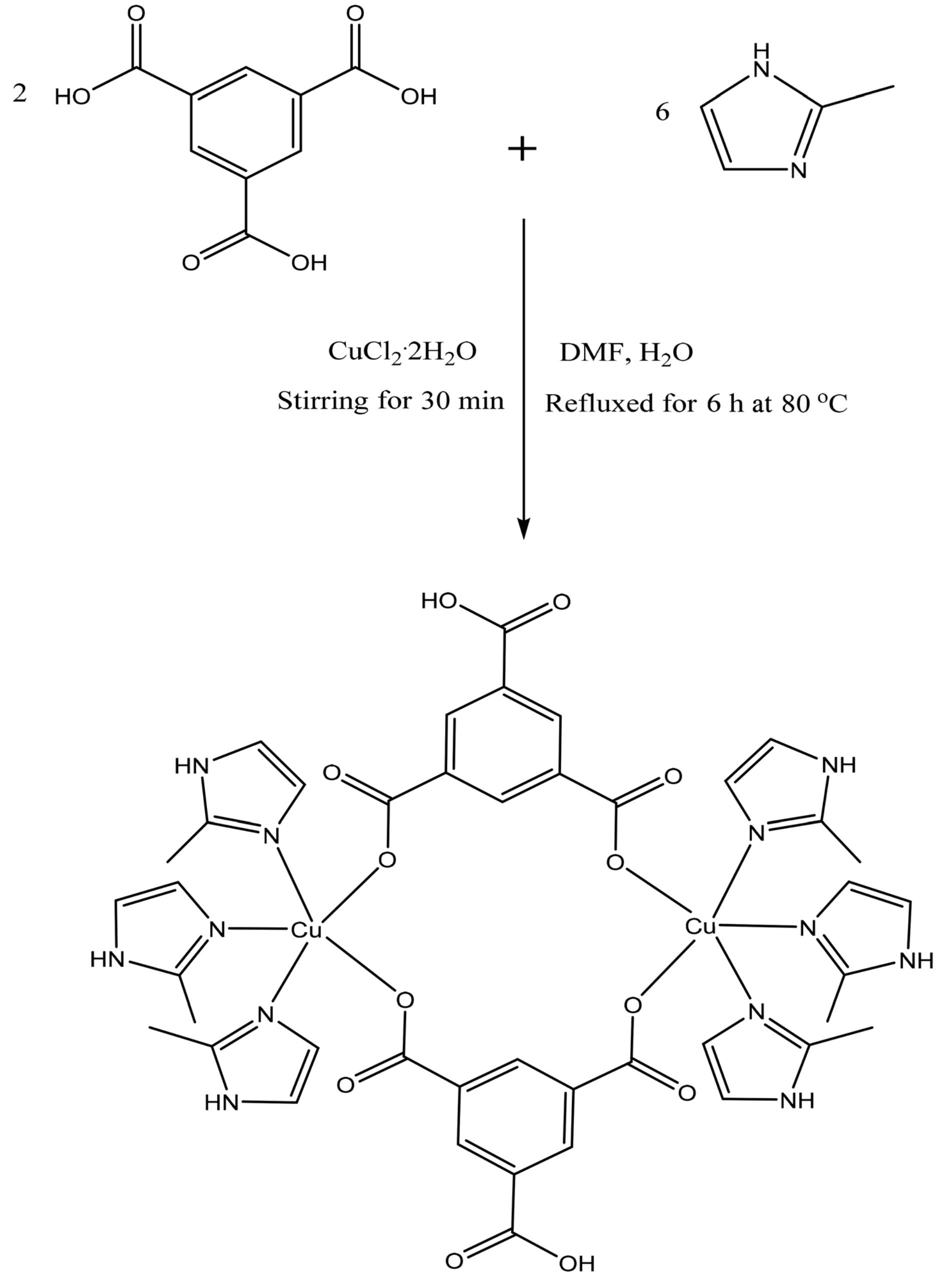

Scheme 2 Chemical synthesis pathway of $[Cu_2(BTA)_2(2\text{-}MeIm)_6]$ MOFs **1**.

2.7. General electrode modification technique

Scientists faced two main obstacles in their quest to improve responsiveness in electrochemical studies: fouling and the gold bare electrode's (AuE) slowness or low response. A variety of techniques have been used to modify AuE, ranging from the fundamental drop-dry procedure to electrodeposition and electro-polymerization. The drop-dry method is controlled by the substrate's adsorption onto the AuE surface, which may lead to a chemical interaction between the substrate and the bare AuE through the chalcogen element (selenium/sulfur). In contrast, the electrodeposition and electro-polymerization processes align the substrates in a regular pattern through intermolecular interactions or direct covalent bonding onto the AuE surface. Throughout this study, bare AuE was modified using a straightforward drop-dry approach. The simple, straightforward, and effective drop-dry method of modifying electrode surfaces is generally used to immobilise nanomaterials onto the surface of the bare gold electrodes. Sulfuric acid and hydrogen peroxide in a ratio of 2 : 1 were used to clean the bare gold working electrode before use. Afterward, it was rinsed with acetone and water and later polished with 0.5 μM alumina paste and cleaned again with ultra-pure water. The cleaned bare electrode was then dried under nitrogen gas.

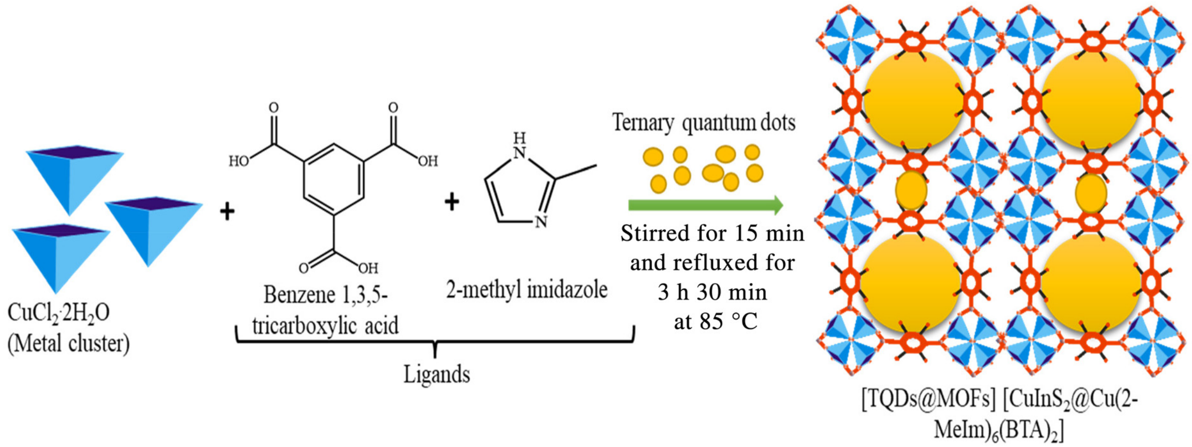

Scheme 3 Graphical synthesis pathway of compound **3**.

5 mg of compound **1** was then dissolved in water with the aid of ultrasonic agitation for 10 min, resulting in a homogeneous suspension. With the aid of a micropipette, some droplets of the suspension were placed at the surface of the cleaned gold electrode. The droplet was allowed to evaporate slowly at room temperature under controlled conditions and later dried under a stream of nitrogen gas. As the solvent evaporated, it left behind a thin layer of the immobilized compound on the gold electrode surface. After drop drying, the modified gold electrode was rinsed with ultrapure water to eliminate any unbound compounds. Finally, the modified electrode was dried under dry nitrogen gas to remove the residual solvent. This procedure of bare electrode modification was applied to **2** and **3** for the electrochemical determination of BPA.

3. Results and discussion

3.1. Molecular structure of compound 1

The ORTEP representation with the atom numbering scheme (without hydrogen and carbon), and the packing diagram of **1** are illustrated in Fig. 1 and 2 respectively. The packing diagram of compound **1** reveals one molecule in the unit cell. Fig. S1 and S2† illustrate the coordination of three molecules of 2-methyl imidazole around each copper(II) ion, which suggests the nearly perpendicular position of two subsequent molecules to the copper(II) ion, and the symmetry by operation of the unit cell, respectively. Fig. S3 and S4† show the projection diagram and polyhedral projection diagram of **1**. Detailed crystallography data and structure refinement parameters are summarized in Table 1; some selected bond lengths and bond angles are presented in Table 2. Compound **1** is a two-dimensional binuclear unit of the copper(II) complex, which is bridged by two molecules of benzene 1,3,5-tricarboxylic acid (BTA) through the anisobidentate-carboxylato oxygens of the bridging ligand, and three molecules of 2-methyl imidazole through the imidazolyl nitrogen atoms coordinated to each copper(II) ion.

The single crystal of compound **1** shows a pentagonal coordination geometry around each copper(II) ion with the chromophore CuN_3O_2. Compound **1** is a centrosymmetric dimer with a pentagonal chair-like conformation at the centre of symmetry as per the reported arrangement for the copper(II) complex.[67] The value of the geometry index or structural parameters for a five coordinate geometry is given using the Tau equation $\tau = (\beta - \alpha)/60$ (β = the first largest angle and α = the second largest angle) which determined whether the five coordinate geometry is square pyramidal (SP) or trigonal bipyramidal (TBP).[68] The value of Tau obtained for **1** is approximately 0.208 which is much closer to null (0) than to unity (1), which confirms that the geometry around the copper(II) ion is distorted square pyramidal with three molecules of 2-methyl imidazole and a molecule of benzene 1,3,5-tricarboxylic acid at the equatorial plane and the second molecule of BTA occupying the axial plane of the molecule. Fig. S5† (the polyhedral ORTEP diagram of **1**) ascertains the geometry deduced through the index parameter Tau. The bond lengths of N1–Cu1, N2–Cu1, N3–Cu1, O1–Cu1, and O3–Cu1 are 1.999(2) Å, 2.002(2) Å, 1.996(2) Å, 2.009(19) Å, and 2.312(2) Å, respectively, which revealed the longer bond length of O3–Cu1 compared to the other four bond lengths, confirming the distortion of the square pyramidal and anisobidentate character of the bridging ligand. The bond lengths observed at the equatorial axes in the range of 1.900 Å to 2.009 Å are comparable to the bond lengths of Cu–N obtained in an ideal square pyramidal geometry which ranges from 1.900 Å to 2.000 Å.[69] The values of adjacent angles at the basal plane of the geometry N3–Cu1–O1 and N2–Cu1–N1 are 86.64° and 88.99°, respectively, and the values of N3–Cu1–N2 and N1–Cu1–O1 are 90.52° and 88.76°. The differences observed in the values of adjacent angles at the basal plane compared to the angles at the basal plane of an ideal square pyramidal geometry further confirmed the distortion of the square pyramidal geometry.[70]

The copper(II) metal–organic frameworks were fictitiously packed at positions "a" and "c" to visualise the inclusion of solvent or small molecules inside the crystal lattice. Small

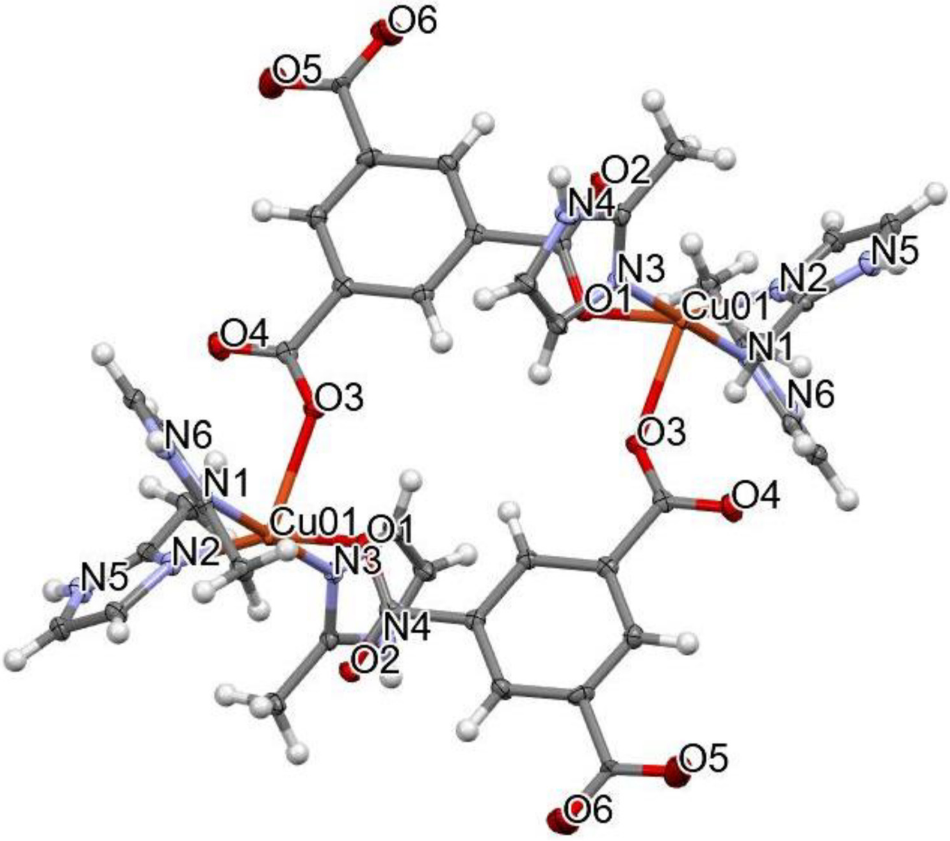

Fig. 1 ORTEP diagram of $[Cu_2(BTA)_2(2\text{-MeIm})_6]$ **1**.

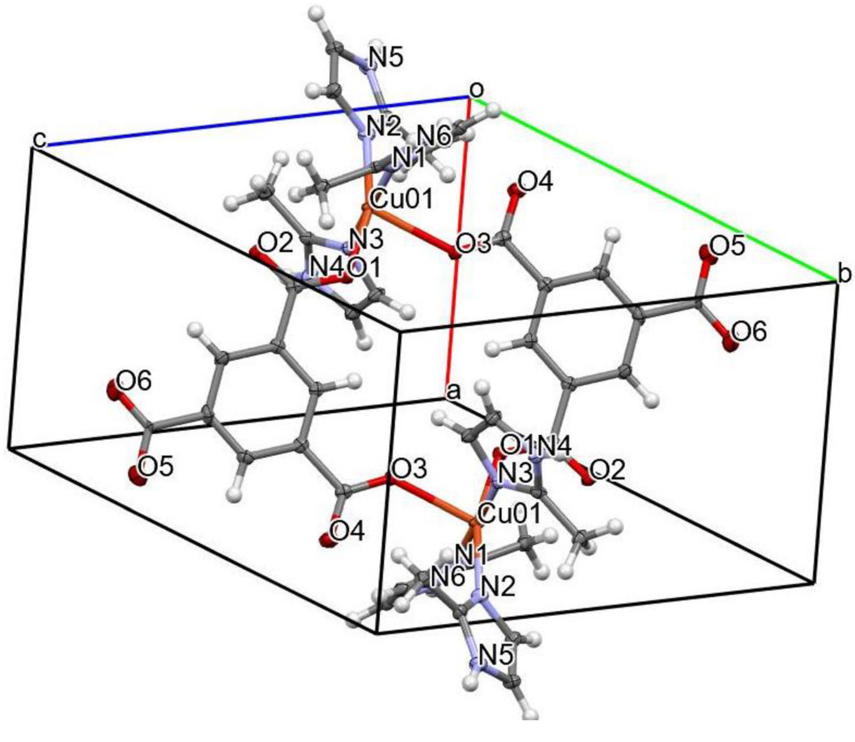

Fig. 2 Packing diagram of $[Cu_2(BTA)_2(2\text{-MeIm})_6]$ **1**.

Table 1 Crystal data and structure refinement of [$Cu_2(BTC)_2(2\text{-MeIm})_6$]

Empirical formula	$C_{42}H_{42}Cu_2N_{12}O_{12}$
Formula weight	1033.95
Temperature/K	100.02
Crystal system	Triclinic
Space group	$P\bar{1}$
a/Å	9.2231(6)
b/Å	11.2106(8)
c/Å	12.2121(8)
α/°	113.068(2)
β/°	100.545(2)
γ/°	91.968(2)
Volume/Å^3	1134.23(13)
Z	1
ρ_{calc}, g cm^{-3}	1.514
μ/mm^{-1}	1.013
F(000)	532.0
Crystal size/mm^3	0.47 × 0.375 × 0.34
Radiation	MoKα (λ = 0.71073)
2θ range for data collection/°	3.71 to 53.584
Index ranges	$-11 \le h \le 11$, $-14 \le k \le 14$, $-15 \le l \le 15$
Reflections collected	48 304
Independent reflections	4847 [R_{int} = 0.0993, R_{sigma} = 0.0548]
Data/restraints/parameters	4847/0/310
Goodness-of-fit on F^2	1.068
Final R indexes [$I \ge 2\sigma(I)$]	R_1 = 0.0458, wR_2 = 0.1255
Final R indexes [all data]	R_1 = 0.0547, wR_2 = 0.1309
Largest diff. peak/hole/e Å^{-3}	0.84/−0.75

Table 2 Selected bond lengths and bond angles of [$Cu_2(BTC)_2(2\text{-MeIm})_6$]

Selected bond angles (°)		Selected bond lengths (Å)	
O(1)–Cu(1)–O(3)	81.94(8)	Cu(1)–O(1)	2.0094(19)
N(3)–Cu(1)–O(1)	86.64(9)	Cu(1)–O(3)	2.312(2)
N(3)–Cu(1)–O(3)	90.53(9)	Cu(1)–N(1)	1.999(2)
N(3)–Cu(1)–N(2)	90.52(9)	Cu(1)–N(2)	2.002(2)
N(3)–Cu(1)–N(1)	178.81(10)	Cu(1)–N(3)	1.996(2)
N(2)–Cu(1)–O(1)	161.73(9)		
N(2)–Cu(1)–O(3)	116.16(9)		
N(1)–Cu(1)–O(1)	94.15(9)		
N(1)–Cu(1)–O(3)	88.76(9)		
N(1)–Cu(1)–N(2)	88.99(9)		

molecules or solvents could be clearly trapped in the crystal pore (Fig. 3). The void space through the contact surface (Fig. 3A) of the crystal was explored at a radius of 0.3 Å and an approximate grid spacing of 0.4 Å. Its volume, 299.54 Å^3, represents 26.4% of the unit cell volume. In addition, the void space through a solvent-accessible surface (Fig. 3B), which was probed at 0.3 Å with a grid spacing of 0.4 Å, had a volume of 153.61 Å^3, equivalent to 13.5% of the unit cell volume.

3.2. Spectroscopy studies of compounds 1–3

3.2.1. FTIR results of compounds 1–3. The FTIR spectra of **1** and the ligands used in the synthesis of compound **1** are presented in Fig. S6(A).† The spectra were compared and assigned after careful comparison which confirms the coordination of the ligands to the copper(II) ion. In the FTIR spectrum of the complex, the bands in the range of 3400–3300 cm^{-1} in the free benzene 1,3,5-tricarboxylic acid (BTA) ligand could be attributed to the carboxylic group which shifted to 3027 cm^{-1}, which confirmed its coordination to the copper(II) ion. The band at 3433 cm^{-1} is assigned to the ν(N–H) stretching frequency in the MOFs, which confirms the coordination of methyl imidazole to the copper(II) ion through the imidazolyl nitrogen. The asymmetric and symmetric carboxylate stretching frequencies were found at 1312 and 1123 cm^{-1} for **1**. The magnitude of the separation $\Delta\nu$ ($\nu_{asym} - \nu_{sym}$) for the carboxylate group in **1** is 189 cm^{-1} which confirms the monodentate coordination of the carboxylate oxygen atoms in **1**.[71] The ν(C=O) in **1** is observed at 1685 cm^{-1} which could be assigned to the carbonyl group present in BTA coordinated to the copper(II) ion. The sharp band at 1640 cm^{-1} could be attributed to ν(C=C) present in the ring of coordinated BTA. The band observed at lower wavelengths of 522 cm^{-1} and 573 cm^{-1} could be assigned to ν(Cu–O) and ν(Cu–N), respectively.[72]

The FTIR spectra of the TQDs and their precursors are presented in Fig. S6(B).† The band at 550 cm^{-1} in the sodium sulfide free compound was blue shifted in the spectrum of the TQDs to 1000 cm^{-1} which indicates interaction between the precursors.[73] The sharp peak observed at about 1500 cm^{-1} in the spectrum of GSH (glutathione) disappeared completely in the spectrum of the TQDs, which indicates interactions between Na_2S and GSH. The bands observed in the spectrum of the TQDs at 1789 cm^{-1}, 3009 cm^{-1}, 3829 cm^{-1}, and 2712 cm^{-1} could be assigned to ν(C=O), ν(O–H), ν(N–H), and ν(S–H), respectively, which are also present in the spectrum of GSH to confirm the presence of the compound in TQDs. The interactions of the copper(II) ion with the sulphur, indium and nitrogen atoms of Na_2S and GSH could be observed at ν(C–S): 479 cm^{-1}, ν(Cu–In): 615 cm^{-1}, and ν(Cu–N): 998 cm^{-1}, confirming the formation of the TQDs.[74,75]

The FTIR spectra of the composite (Fig. S7†) revealed similar stretching vibrations observed in the spectra of the MOFs and TQDs which confirmed the formation of the composite. The ν(C–S), ν(Cu–O), ν(Cu–In), and ν(Cu–N) bands in the spectrum of the composite at 479 cm^{-1}, 552 cm^{-1}, 615 cm^{-1}, and 998 cm^{-1} were observed in the spectra of the MOFs and TQDSs. The broad band observed at around 3500–2700 cm^{-1} could be assigned to the ν(O–H) and ν(N–H) stretching frequency in the spectra of the MOFs and TQDs, respectively.

3.2.2. Electronic studies of compounds 1–3. The electronic spectra of compounds **1–3** are presented in Fig. S8(A), (B), and (C)† respectively. Compound **1** has four major absorption bands. The band observed at 222 nm could be assigned to the π → π* charge transfer transitions of the aromatic ring in benzene 1,3,5-tricarboxylic acid coordinated to the Cu(II) ion.[76] The three other absorption bands observed at 439 nm, 500 nm, and 549 nm could be attributed to the d → d transition of the Cu(II) ion, ligand to metal charge transfer (LMCT) between benzene 1,3,5-tricarboxylic acid and the Cu(II) ion, O(pπ) → Cu(dπ*), and the metal to ligand charge transfer between the Cu(II) ion and 2-methyl imidazole, Cu(dπ) → N(pπ*).[77,78]

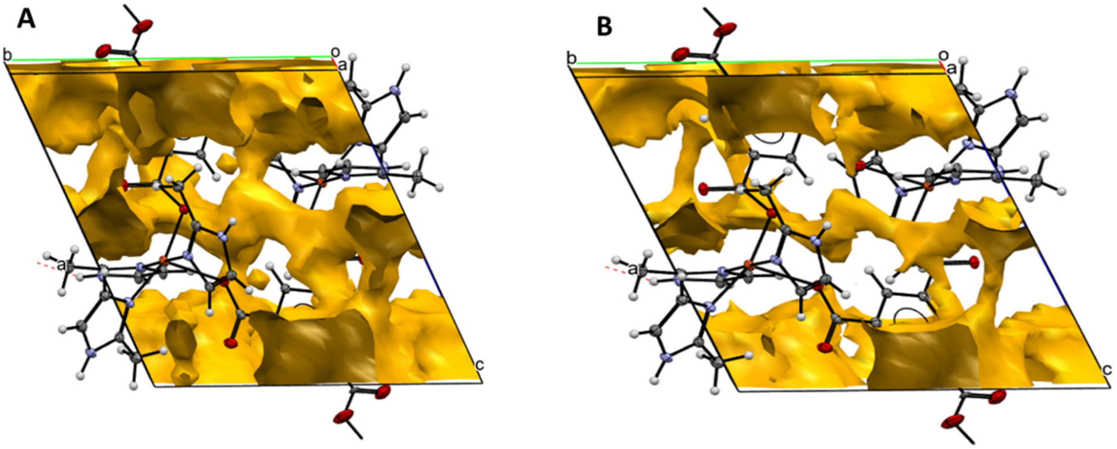

Fig. 3 Void space of $[Cu_2(BTC)_2(2\text{-MeIm})_6]$ **1** through the contact surface (A), and solvent accessible surface (B).

The electronic spectrum of compound **2** revealed two major absorption bands. The band at 265 nm could be attributed to the n → π* charge transfer transition within glutathione and the absorption band seen at 516 nm could be assigned to ligand to metal charge transfer (LMCT) between glutathione and the Cu(II) ion, $N(p\pi) \rightarrow Cu(d\pi^*)$.[79]

Compound **3**, which is the composite of **1** and **2**, shows the various absorption bands present in **1** and **2** with slight shifts. The two major bands observed in **3** are 405 nm, which is a blue shift of the absorption band observed in **1** (439 nm), and 263 nm, which is also a blue shift of the absorption band observed in **2**. This shift of absorption bands in **3** from those observed in **1** and **2** simply suggests the interaction of **2** which is encapsulated in **1**.[80]

3.3. Morphological studies of compounds 1–3

The morphology, topology, size distribution and inner structure of these compounds were studied using scanning electron microscopy (SEM) and transmission electron microscopy (TEM). The SEM micrograph of the metal–organic framework **1** shows a heterogeneously dispersed rough surface morphology with a granular structure with sizes ranging between 1 and 50 nm (Fig. 4A1), and the TEM micrograph shows well-defined flakes of cubic shape which gives more insight that the compound is highly crystalline, with the particle size in the range of 10–50 nm, with an average particle size of 21.3 nm obtained from the histogram of SEM in the inset (Fig. 4A2).[81] Through the SEM micrograph of **2** (Fig. 4B1), it could be observed that the particles of **2** are homogeneous, and have a spherical particle structure with a smooth surface. These particles have a grain-like morphology and are agglomerated with sizes ranging from 1 to 50 nm with an average particle size of 1.27 nm in the histogram of SEM in the inset. The TEM micrograph (Fig. 4B2) reveals a spherical scaled shape of particles. These particles have uniform structures and shapes, which reveals the properties of **2** that could aid in enhancing the electrochemical response of the composite when encapsulated in **1**.[82]

The SEM micrograph of composite **3** (Fig. 4C1) shows a rough surface with underlying aggregation of the particles of **2** encapsulated in the void spaces of **1**. The surface of **3** is distributed with countless monodisperse particles with sizes ranging from 1 to 50 nm, which could provide more reactive sites with a favourable response in the electrochemical process. More detailed information on **3** is further provided by TEM "C2" (Fig. 4C2), and it is clear that the composite consists of cubic particles with particle sizes similar to that of **1** with an average particle size of 23 nm from the histogram graph of SEM in the inset. It could also be seen from the TEM micrograph of **3** that the particles are randomly distributed, which could be the particles of **2** encapsulated in the pores of **1**.[83]

The electrical conductivity of these compounds was studied by calculating their band gap energy. These optical band gaps were obtained using the plot $(\alpha h\nu)(1/\gamma)$ *vs.* $h\nu$, where α is the absorption coefficient, h is the Planck constant, ν is the photon frequency, and $(1/\gamma)$ is the electron transition factor, which is $\frac{1}{2}$ in this study for the direct band gap.[84,85] The various band gap energy values obtained are 5.36 eV, 3.96 eV, and 3.82 eV for compounds **1–3** respectively, which indicate a red shift in the wavelength of these compounds, respectively,[86] and a confinement of these compounds with respect to other semiconductors such as CdS, CdSe, CdTe, PbSe, InP, and InAs.[87] The lowest band gap energy value obtained for the composite (3.82 eV) indicates that this compound has high electrical conductivity compared to the individual MOFs and TQDs[88] (Fig. S8D†).

3.4. Fluorescence study of compounds 1–3

The fluorescence properties of these compounds were studied in order to investigate their responses in the presence of BPA. 5 mg of each compound was dissolved in 8 mL of dimethylsulfoxide (DMSO) and subjected to various concentrations of the preferred analyte. These compounds were excited at 325 nm with the emission wavelength ranging between 320 nm and 550 nm, a slit width of 10 nm, and the voltage considered for this study being 800 V. Various BPA concen-

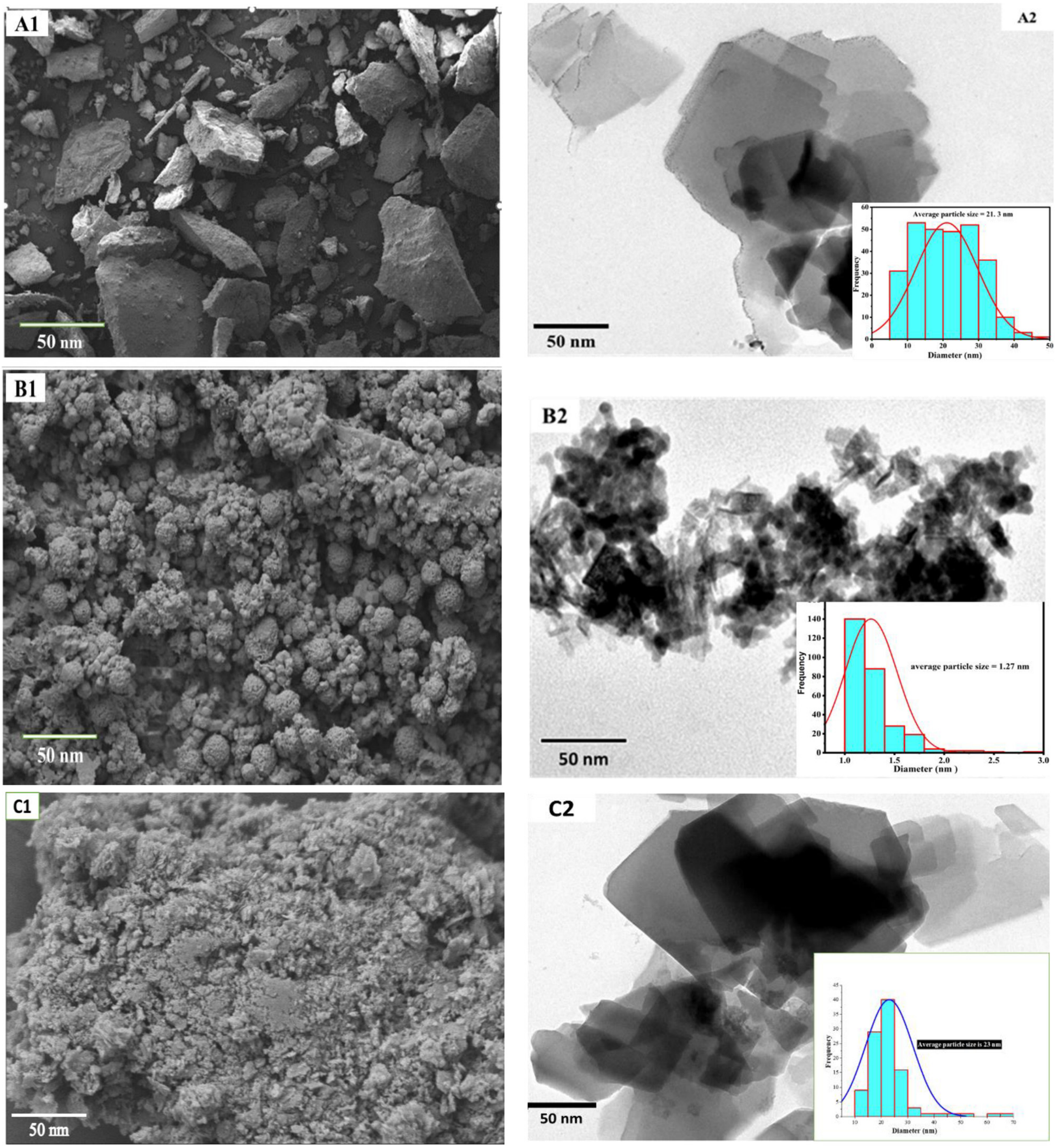

Fig. 4 SEM micrographs of compounds **1–3** respectively presented as A1, B1, and C1, and the TEM micrographs of compounds **1–3** respectively presented as A2, B2, and C2. The inset is the average particle sizes of compounds **1–3** presented as C1, C2, and C3, respectively.

trations were prepared ranging between 2 nM and 14 nM and were examined. A single fluorescence emission peak was observed for the three compounds at different wavelengths, and the fluorescence emission intensity peak of each compound increased as the concentration of the preferred analyte increased, suggesting an enhanced response of the fluorescence ability of each compound in the presence of the preferred analyte (BPA) (Fig. 5A–C). Compound **1** exhibited a violet fluorescence emission band at 380 nm ($\lambda_{\max}$ = 325 nm), which could be attributed to (Oπ → pπ*), the transition of charge between the ligand and the copper(II) ion with a relative fluorescence intensity at 140 W m^{-2} (watt per square metre) for 14 nM BPA (Fig. 5A).[89] Compound **2** also revealed a violet fluorescence emission band at 348 nm ($\lambda_{\max}$ = 325 nm), which

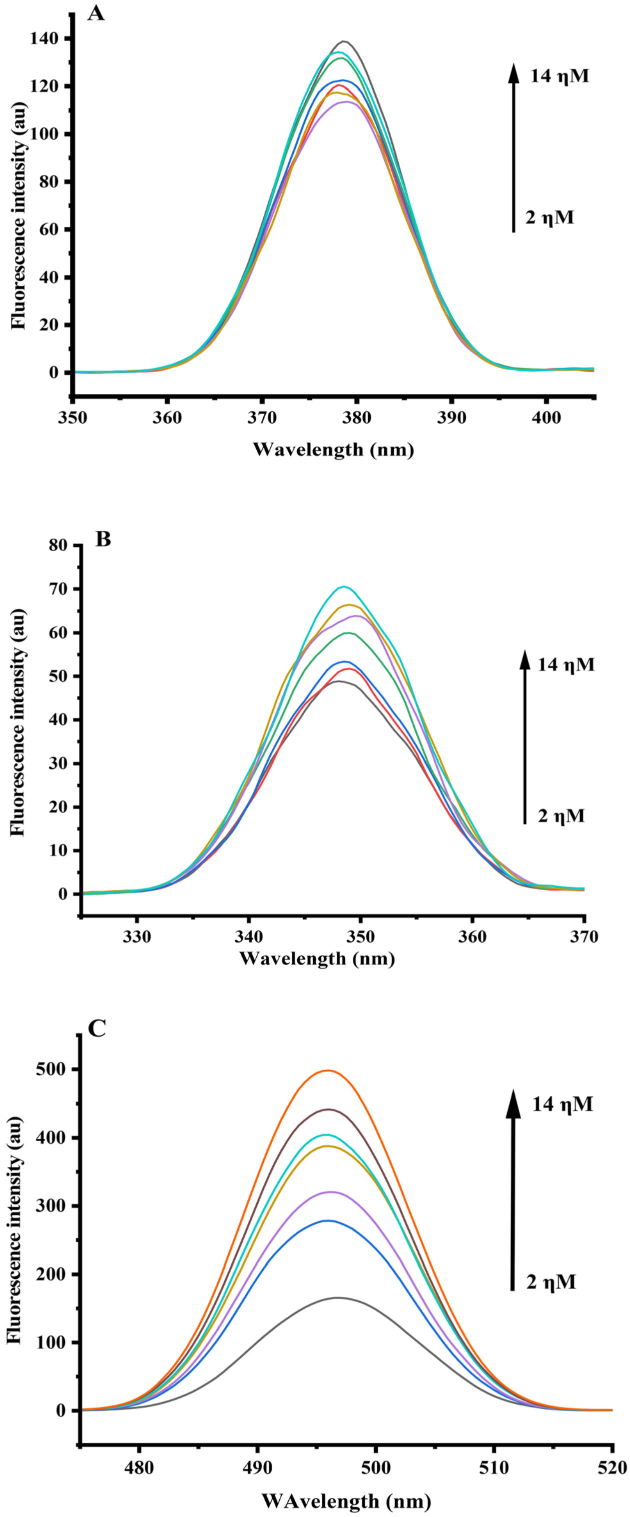

Fig. 5 Florescence responses of the electrodes modified with compounds **1–3** presented as (A), (B), and (C), respectively.

could be assigned to the intraligand ($\pi \rightarrow \pi^*$) transition of glutathione with a relative fluorescence intensity peak found at around 71 W m^{-2} for 14 nM BPA (Fig. 5B).[90] Compound **3** shows a blue fluorescence emission band at 498 nm (λ_{max} = 325 nm), with a relative fluorescence intensity at around 500 W m^{-2} for 14 nM BPA (Fig. 5C). This transition of the fluorescence emission colour from violet to blue, increase in the fluorescence emission band to 498 nm, and enhancement in the fluorescence intensity (500 W m^{-2}) suggest a positive interaction between the MOFs and TQDs encapsulated into their pores and a faster recombination of the photogenerated electron–hole pair of the composite. The synergistic effect of the fluorescence responses of each of the MOFs and TQDs facilitated and enhanced the fluorescence of the composite in the presence of BPA compared to the fluorescence intensity of each of the MOFs and TQDs.

3.5. Cyclic voltammetry responses of 5 mM potassium ferricyanide [$K_3(Fe(CN)_6)$] in 0.1 M potassium chloride (KCl) at the surface of bare and gold electrodes modified with compounds 1–3 at pH 7

Potassium ferricyanide [$K_3Fe(CN)_6$] is a red redox probe salt composed of the [$Fe(CN)_6$]$^{3-}$ coordination compound, which is water soluble and exhibits fluorescence. [$K_3Fe(CN)_6$] is used as a tool in electrochemical experiments and it consists of an octahedral [$Fe(CN)_6$]$^{3-}$ centre cross-linked with the K^+ ion bound to the CN^- ligand and was chosen for its surface-sensitive electrochemical response, especially for the gold electrode.[91] Fig. 6 illustrates the cyclic voltammetry (CV) responses of [$K_3(Fe(CN)_6)$] at pH 7 at the surface of the various electrodes (bare electrode and electrodes modified with compounds **1–3**) obtained at different scan speeds (100 mV s^{-1}–325 mV s^{-1}). The CV responses of [$K_3(Fe(CN)_6)$] were obtained over a potential window sweep of −0.2 V to 1.0 V, and redox reactions (responses) were performed at the surface of the bare and modified electrodes. The oxidation peak current (I_{pa}), the reduction peak current (I_{pc}), and the potential peak separation ΔE_p ($\Delta E_p = E_{pa} - E_{pc}$, where E_{pa} is the oxidation peak potential and E_{pc} is the reduction peak potential) are presented in Table 3.

Observing the changes in the CV responses of [$K_3(Fe(CN)_6)$] at the electrodes modified with compounds **1–3** (Fig. 6B–D, respectively) compared to that of the bare electrode (Fig. 6A), a successful modification of the bare gold electrode with compounds **1–3** was ascertained. For all the modified electrodes, an increase in the scan rate of the reaction leads to an increase in the redox peak current response (I_{pa} and I_{pc}), and a plot of the applied potential (V) at the surface of these modified electrodes *versus* the square root of the scan rate ($\upsilon^{1/2}$), which gives a linear regression, as shown in the inset; the slopes obtained for the linear regressions for all the modified electrodes, which are less than 1, indicate that these electrochemical processes at the surface of these modified electrodes are diffusion controlled.

From Table 3, it could be observed that the electrode modified with compound **3** has the highest oxidation peak current (5.273×10^{-4} μA) and a low separation peak potential ΔE_p (198 mV) compared to the electrodes modified with compounds **1** and **2**. In accordance with Nicholson's theory, a decrease or a low magnitude of the separation peak potential ΔE_p (less than 300 mV) instigates an increase in the hetero-

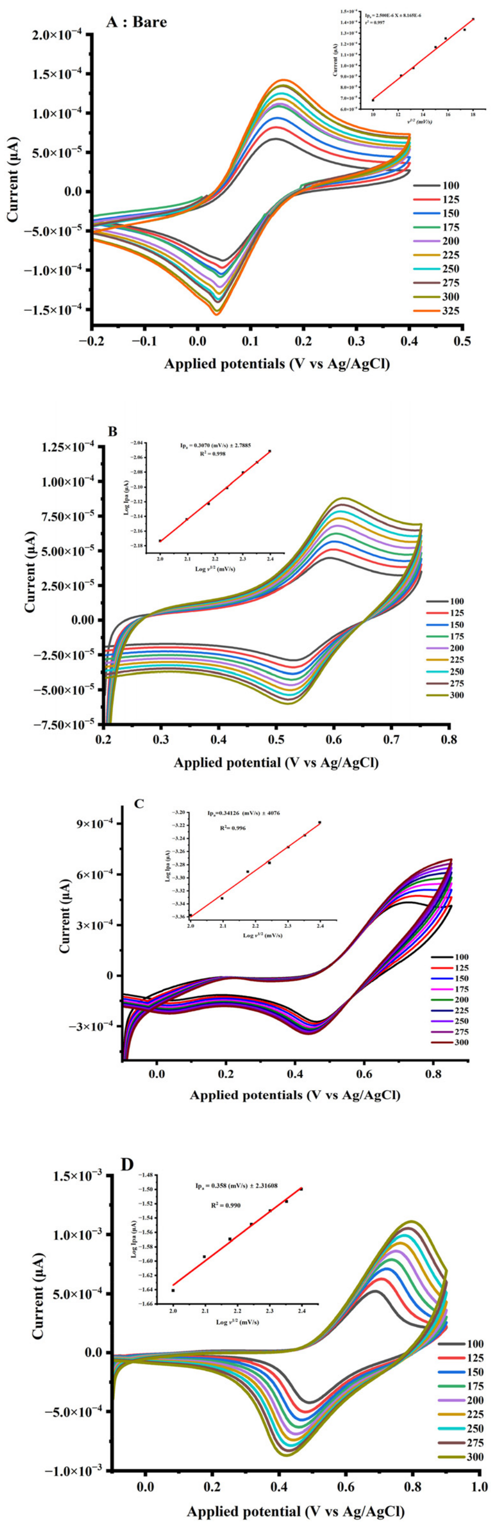

Fig. 6 Cyclic voltammetry curves of $[K_3Fe(CN)_6]$ at different scan rates (100 mV s^{-1}) for the bare electrode (A), and the electrodes modified with compounds **1** (B), **2** (C), and **3** (D).

geneous rate constant (k°) which signifies fast movement of electrons or transfer of large numbers of electrons between the surface of the electrode modified with compound **3** and $[K_3(Fe(CN)_6)]$.[92] The distorted square pyramidal geometry of **1** which is the host compound after encapsulating **2** could alter its orbital energy and lead to an increase in the redox potential and fast movement of electrons. The nitrogen donor atom of the ligand (2-MeIm) that leads to the formation of a sigma donor (σ-donor), and sometimes a pi-acceptor (π-acceptor), stabilizes the oxidation of the analyte, causing an excellent interaction between the composite and the analyte and leading to a low magnitude of the separation peak potential experienced. To further confirm the large surface area of the composite modified electrode in contrast to the electrodes modified with compounds **1** and **2**, the Randles–Sevcik equation was used[93] (eqn (1) and (2)).

$$I_{\text{pa}} = 2.69 \times 10^5 A D^{\frac{1}{2}} n^{3/2} \nu^{1/2} C \tag{1}$$

$$A = \frac{I_{\text{pa}}}{\left(2.69 \times 10^5 n^{\frac{3}{2}} D^{\frac{1}{2}} C \nu^{\frac{1}{2}}\right)} \tag{2}$$

Here, I_{pa} is the oxidation peak current, A is the surface area of the modified electrode, D is the diffusion coefficient of $[Fe(CN)_6]^{3-}$ (7.6×10^{-6} cm^2 s^{-1}), C is the bulk concentration of $[K_3(Fe(CN)_6)]$, n is the number of electrons, and ν is the scan rate.

After substituting the appropriate values for the calculation of the surface area (A) for the electrodes modified with compounds **1–3**, using the Randles–Sevcik equation, it was found that 'A' values were 254.24 mm^2, 311.84 mm^2, and 345 mm^2, respectively. The high surface area of the composite modified electrodes resulted in a higher oxidation peak current potential and excellent electron transfer rate compared to the other modified electrodes.

3.6. Electrochemical impedance spectroscopy (EIS)

In a standard electrochemical cell, besides the resistance of the electrolyte, redox species (matter–electrode) connections include the concentration of electroactive species, charge-transfer, and mass-transfer from the bulk solution to the surface of the electrode. Electrical circuits, which comprise resistors, capacitors, or constant phase components coupled in series or parallel, were designed to create an equivalent circuit that defines each of these parameters.[94] Therefore, EIS could be used to explore mass-transfer, charge-transfer, and diffusion processes because of its ability to study intrinsic material properties or specific processes that could influence the conductance, resistance, and capacitance of an electrochemical system, which are observed through the electrode responses. This analysis of impedance data for the reduction of ferricyanide in the potassium chloride (KCl) supporting electrolyte illustrates the error structure for impedance measurement, the use of measurement, the process methods, and the sensitivity of impedance to the evolution of electrode characteristics.[95] The standard redox probe used in our research is 5 mM potassium ferricyanide in 0.1 M potassium chloride with the application of a frequency ranging from 0.1 Hz to 100 KHz. Nyquist plots were used to obtain impedance across the modified electrodes (Fig. 7A–D). The data obtained

Table 3 Summary of the cyclic voltammetry results of $[K_3Fe(CN)_6]$ obtained at the surface of the electrodes modified with compounds **1–3** at 100 mV s^{-1}

	Oxidation response		Reduction response		
Modified electrodes	I_{pa} (μA)	E_{pa} (V)	I_{pc} (μA)	E_{pc} (V)	Potential separation ΔE_p (V) = $E_{pa} - E_{pc}$
MOFs/AuE	4.53×10^{-5}	0.594	-2.84×10^{-5}	0.661	0.066
TQDs/AuE	4.42×10^{-4}	0.725	-2.669×10^{-4}	0.469	0.256
TQDS@MOFs/AuE	5.273×10^{-4}	0.691	-4.282×10^{-4}	0.493	0.198

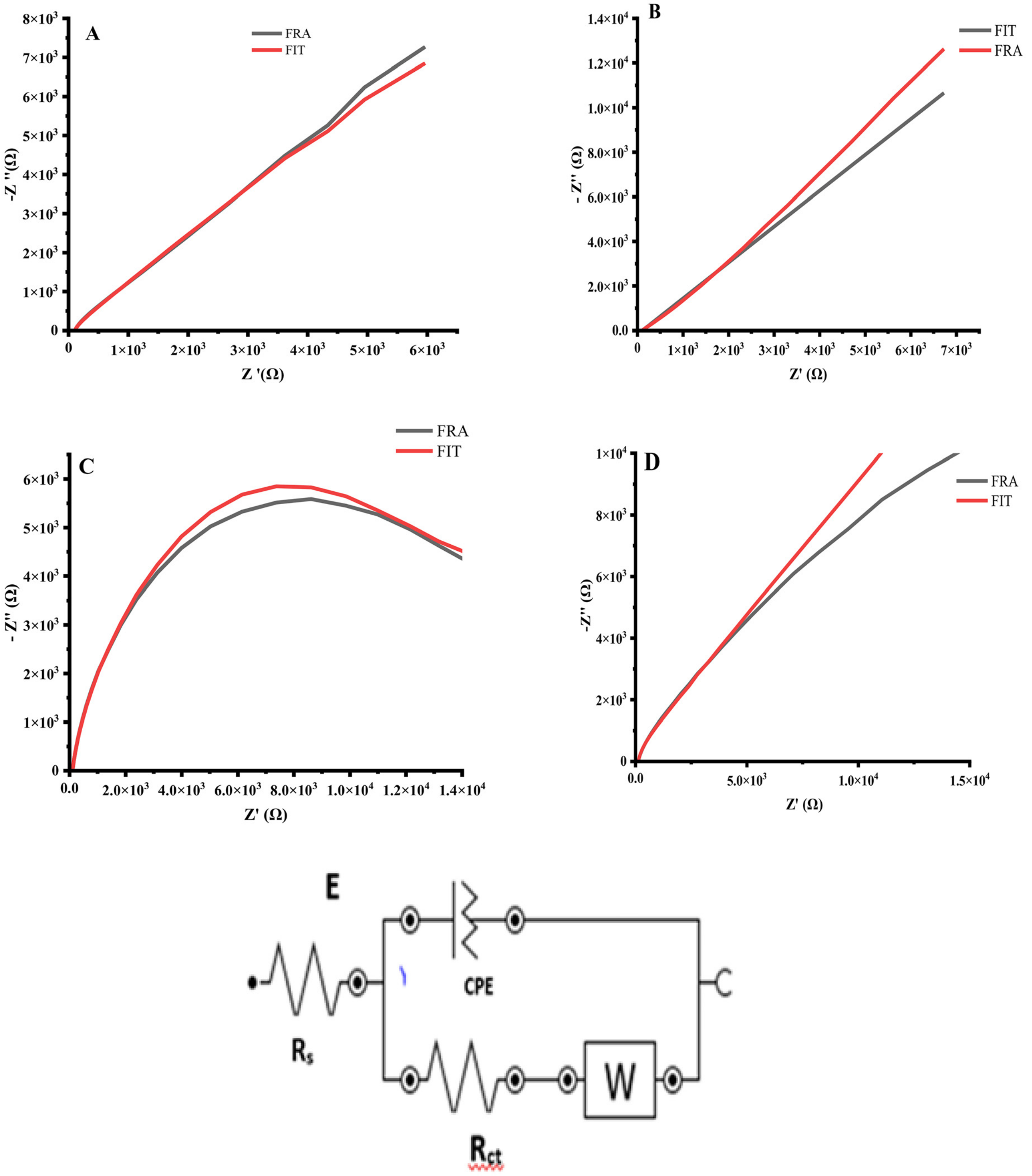

Fig. 7 Nyquist plots obtained for 5 mM $[K_3Fe(CN)_6]$ in 0.1 M KCl prepared in PBS solution pH 7, using the bare electrode (A), and electrodes modified with compounds **1** (B), **2** (C), and **3** (D), and the equivalent Randles–Sevcik circuit used in the EIS experiments (E).

were validated through the low error (n) values, which is the difference between the experimental data and the fitted data. For the interpretation of the impedance spectra obtained, an equivalent Randles–Sevcik circuit is used, which is made up of electrolyte resistance (R_s), charge transfer resistance (R_{ct}), the constant phase element (CPE) or double layer capacitance (C_{dl}), and the impedance of the Faradaic reaction (Z_w) which is also known as the Warburg impedance or the diffusional resistance element (Fig. 7E). When a Faradaic reaction takes place, the reaction occurs in parallel with the charging of the double layer and the rate of the Faradaic reaction is controlled by diffusion of the reactant to the electrode surface, which is illustrated by a straight line with an angle of 45° in the low frequency region.[96] When a non-Faradaic reaction occurs, the reaction is not parallel with the charging of capacitance and the rate of the Faradaic reaction is controlled by the adsorption of the electrolyte particles to the surface of the electrode, which is observed by a semi-circle or an arc signifying the limitation of charge transfer or impedance.[97] The values of charge transfer resistance (R_{ct}) obtained at the surface of the electrodes modified with compounds **1–3** in 5 mM [$K_3Fe(CN)_6$] are 5.12 kΩ, 14.1 kΩ, and 22.2 mΩ, respectively. These results show that the electrode modified with compound **3** has the highest rate of electron transfer due to the lowest R_{ct} value (Table 4).

The exponent values correlated with the degree of ideality in the capacitive behaviour of the system which are less than unity (n < 1) for all the modified electrodes, indicating the non-homogeneous nature of the gold electrode. These values range from 0.650 to 0.980.[98] The phase shift angles of all the electrodes, bare and modified with compounds **1–3**, in the Bode plots (Fig. 8) are 51.57°, 53.81°, 53.29°, and 66.44°, respectively. These values are less than 90 °C, which showed that the modification of the electrodes is non-capacitive.[99]

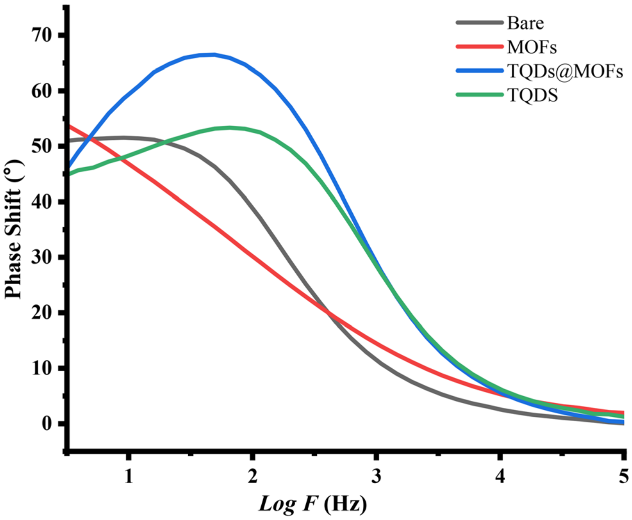

Fig. 8 Bode plots obtained at the surface of the bare electrode and electrodes modified with compounds **1** MOFs, **2** (TQDs), and **3** (TQDs@MOFs).

4. Electrochemical determination of BPA using cyclic voltammetry

Cyclic voltammetry (CV) is a type of potentiodynamic measurement in electrochemistry that is used to study the electrochemical properties of an analyte in solution, or a molecule that is adsorbed onto the electrode or interacts with the surface of the electrode. The electrochemical behaviour of BPA at the surface of the electrodes modified with compounds **1–3** is illustrated in Fig. 9. A concentration of 5 μM BPA at pH 7 was prepared for this study at different scan rates (100 mV s^{-1} to 300 mV s^{-1}). Different responses were recorded at the surface of the electrodes modified with compounds **1–3**, and are illustrated in Fig. 9(A), (B), and (C), respectively. The potential window used for this study differs for modified electrodes. For the electrode modified with compound **1** the potential window was recorded between −0.5 V and 1.1 V, for the electrode modified with compound **2** the response was observed in the potential window range of −0.3 V to 0.4 V, and for the electrode modified with compound **3**, the response was observed in the potential window range of −0.2 V to 1.2 V. A redox reaction (redox peak current) was experienced at the surface of electrodes modified with compounds **2** and **3** (Fig. 9B and C), which indicate that at these electrodes, the reaction was completely reversible, while at the electrode modified with compound **1**, only an oxidation reaction was observed, which implies an irreversible reaction ($I_{pa}/I_{pc} \neq 1$). The linear relation between the oxidation peak current (I_{pa}) and the square root of the scan rate ($v^{1/2}$) is presented in the inset. For electrodes modified with compounds **2** and **3**, an increase in the scan rate leads to an increase in the oxidation peak current, indicating that the electrochemical response of BPA at the surface of

Table 4 Electrochemical impedance spectroscopy data obtained for 5 mM [$K_3Fe(CN)_6$] in 0.1 M KCl obtained at the bare electrode, and electrodes modified with compounds **1–3**

Au electrode	R_s (Ω)	R_{ct} (kΩ)	Z_w (μMho)	CPE (mS) (μMho)	n
Bare electrode	106	52.7	125	16.6	0.855
Electrode modified with compound **1**	108	5.12	2.20	105	0.864
Electrode modified with compound **2**	101	14.1	298	8.85	0.84
Electrode modified with compound **3**	163	22.8	42.7	8.85	0.98

"n" the exponential related to the depression angles.

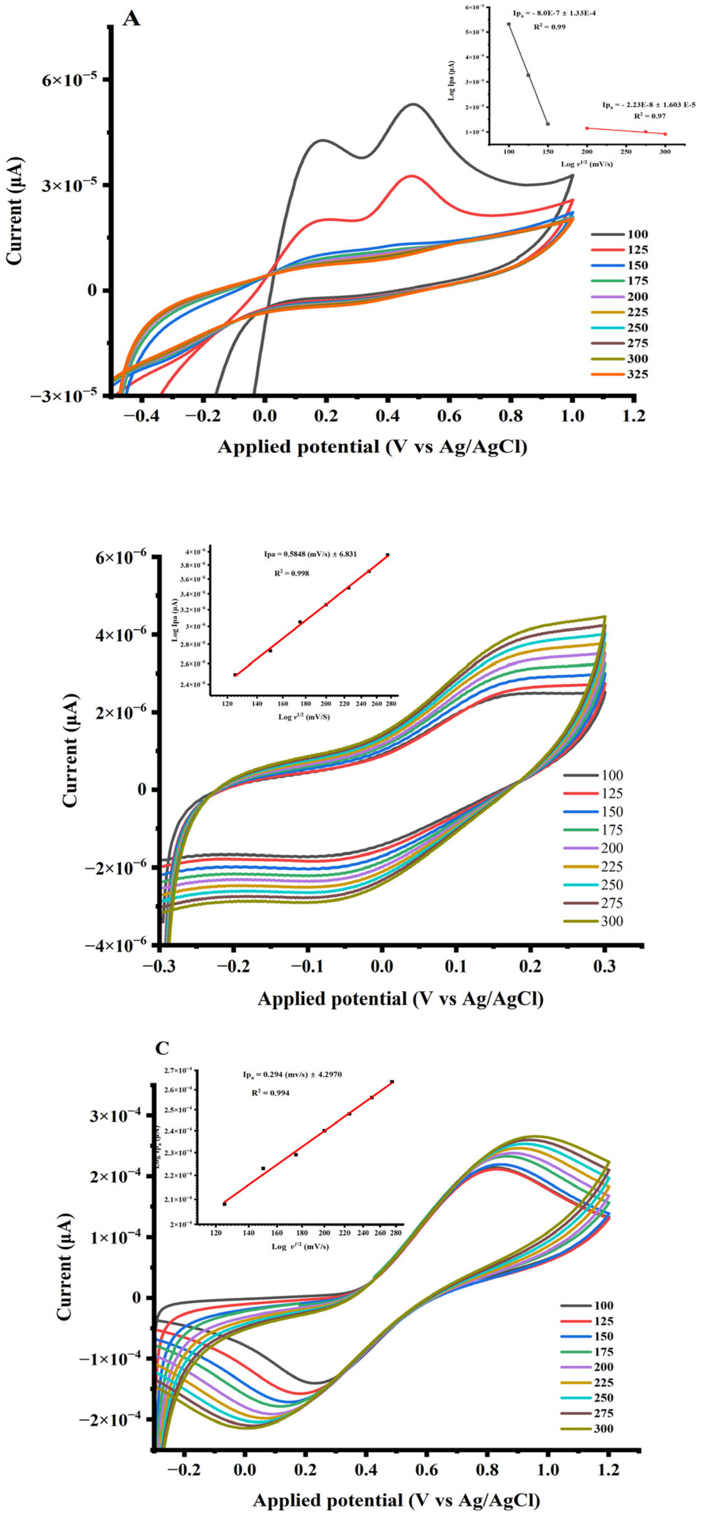

Fig. 9 Electrochemical determination of BPA at the surface of the electrodes modified with compounds **1** (A), **2** (B), and **3** (C) using cyclic voltammetry.

these electrodes is diffusion controlled with slopes ranging between 0.2 and 1.0, while at the electrode modified with compound **1**, there is a decrease in the oxidation peak current as the scan rate increases, which implies that the surface of the electrode is getting fouled by agents that form an increasingly impermeable layer on the electrode surface, inhibiting the direct contact of BPA with the surface of the electrode for continuous electron transfer.[100] Table 5 presents the responses

Table 5 Summary of the electrochemical responses (I_{pa}, I_{pc}, E_{pa}, E_{pc}, and ΔE_p) at a scan rate of 300 mV s^{-1} obtained at the surface of the electrodes modified with compounds **1–3**

	Electrode modified with **1** (MOF)	Electrode modified with **2** (TQDs)	Electrode modified with **3** (TQDs@MOFs)
I_{pa}	1.20×10^{-5}	4.174×10^{-6}	2.70×10^{-4}
I_{pc}	—	-2.89×10^{-6}	-2.16×10^{-4}
E_{pa} (V)	0.590	0.201	0.951
E_{pc} (V)	—	−0.072	0.012
$\Delta E_p = (E_{pa} - E_{pc})$ (V)	0.590	0.273	0.939

observed (I_{pa}, I_{pc}, E_{pa}, E_{pc}, and ΔE_p) at the surface of all the modified electrodes at a scan rate of 300 mV s^{-1}. From the table, it could be confirmed that the highest oxidation peak current (2.70×10^{-4} μA) at the surface of the modified electrodes is observed at the electrode modified with compound **3**. This excellent performance could be attributed to the volume of the pore of the synthesized MOFs, which is 299.54 Å^3 through the contact surface and 1.5361 Å^3 through the solvent accessible surface, which are voluminous to encapsulate the TQDs with an average particle size of 1.27 nm. The tunability feature of these MOFs encapsulated with TQDs enables specific chemical interactions, enhanced transduction, and optical or electrochemical interactions. The pore size and tunability of these MOFs encapsulated with TQDs therefore ensure a high surface area, high selectivity, a fast response, and high stability, making TQDs@MOFs an excellent composite for BPA detection. Therefore, this electrode modified with **3** will facilitate the movement and large transfer of electrons between the preferred analyte and the composite at the surface of the modified electrode due to its large surface area (A), which indicates higher adsorption capacity and interaction, electrochemical conductivity, and electrochemical properties (intra and intermolecular attraction) through the synergistic interaction between the MOFs and TQDs[101] (Fig. S9†). A schematic representation of the oxidation of BPA at the surface of the modified electrode is presented in Fig. S10.† This reaction mechanism generates a reliable signal, which is the basis of detection through the voltammetric parameter, and the modified electrode could also be cleaned or refreshed with an appropriate solvent under favourable conditions to maintain its efficiency. However, long term application without cleaning the surface of the electrode could cause the fouling of the electrode surface, caused irreversible surface modification, deterioration or decay or loss in the sensitivity of material recognition.

4.1. Optimization of analytical parameters

Determining the ideal experimental conditions for maximum sensitivity requires optimising the BPA accumulation characteristics on the modified electrode surface. The various analytical parameters considered for the BPA optimization were pH, time of reaction upon contact of BPA with modified electrode, the scan rate, and the concentration of the composite at the surface of the modified electrode.

4.1.1. pH. The pH of the solution employed is a crucial parameter to consider in the optimum determination of BPA, since the oxidation potential and peak current in detecting BPA are affected by shifts in the redox peak potential towards more positive and negative orientations with lower and higher pH values, respectively.[102] PBS buffer solutions with a pH range between 2 and 12 with a gradient range of 0.5 were prepared for this study in which the solution of preference will be dissolved for its determination. The results shown in Fig. 10(A) reveals that when the pH of the PBS buffer solution reached 7, the oxidation peak current value reached the maximum. Therefore, pH 7 (neutral pH) which shows better performance was chosen as the optimal pH value for this study. Besides, the oxidation peak potential of BPA shifted towards negative values with an increase in pH. The linear regression equation for the pH dependence of E_{pa} is given in eqn (3):

$$E_{pa} = -0.0627\ \text{pH} \pm 0.9574 \quad (R^2 = 0.9926) \tag{3}$$

The absolute value of the slope "−0.06194 V" per unit pH is approximately near 0.059 V per unit pH, suggesting that the number of electrons transferred is equivalent to the number of protons in the electrooxidation of BPA at the electrode modified with compound **3**.[103]

4.1.2. Time of reaction upon contact. The influence of contact time for BPA detection on the surface of the electrode modified with compound **3** was investigated and the results are shown in Fig. 10(C). The modified electrode could attain maximum detection in an effective state with the right amount of contact time. An excessive amount of contact time may cause the BPA particles to reoccur at the surface of the modified electrode and waste time, whereas an inadequate amount of contact time may allow the composite on the electrode surface to insufficiently detect BPA particles in the solution, leading to low detection. As the contact time increases between 0 and 10 min, the oxidation peak current (I_{pa}) also increases and attains a plateau at 5 min. A further increase in contact time resulted in the decrease of the oxidation peak current, which later became relatively stable. This could be due to the saturation of the modified electrode surface, which impedes more BPA particles from being detected. Therefore, 5 min was selected as the optimum contact time for the efficient detection of BPA.

4.1.3. Scan rate. The influence of the scan rate on the electro-oxidation determination of BPA is seen in Fig. 10(C). It can be observed that the oxidation peak current linearly increases with an increase in the scan rate (100 mV s^{-1}–300 mV s^{-1}), and a good relationship between the oxidation peak current and the scan rate is observed. The linear relation-

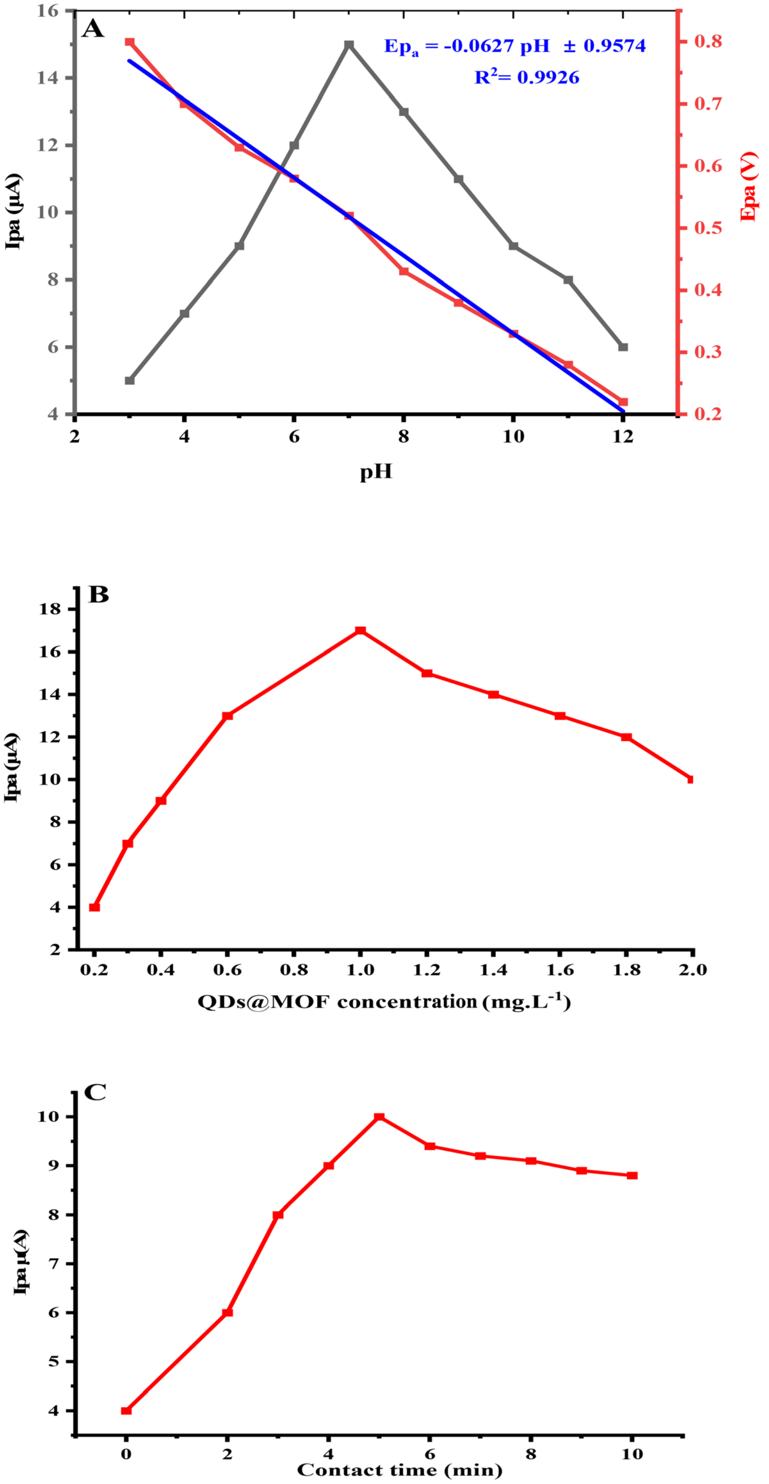

Fig. 10 Effect of PBS, pH, contact time and optimal concentration of [CuInS$_2$@Cu(2-MeIm)$_6$(BTA)$_2$]/AuE for the electrochemical sensing of BPA.

ship could be expressed as: I_{pa} = 0.294 (mV s^{-1}) ± 4.2970 (R^2 = 0.994), which indicates that the determination of BPA at the surface of the electrode modified with **3** is diffusion controlled, (slope 0.294 is closer to 0.5).[104]

4.1.4. Composite concentration at the surface of the modified electrode. The concentration of the composite dropped at the surface of the modified electrode also affects its performance. A high concentration could lead to a poorly dispersed cluster of composites on the electrode, and a low concentration could result in deficient detection due to fewer composite particles on the electrode surface. Therefore, different concentrations of composite ranging from 0.2 mg L^{-1} to 2.0 mg

L^{-1} were prepared, and 4 μL of these concentrations was added dropwise at the surface of the modified electrode to carry out this experiment. It could be observed from Fig. 10(B) that as the concentration of the composite increases, the oxidation peak current also increases and reaches a maximum when the concentration of the composite on the modified electrode is 1.0 mg L^{-1}, after which an increase in the concentration resulted in a decrease of the oxidation peak current. It could then be concluded that 1.0 mg L^{-1} is the most adequate composite concentration for effective and efficient BPA detection.

4.2. Determination of BPA at the surface of the electrodes modified with compounds 1–3 using differential pulse voltammetry (DPV)

Differential pulse voltammetry (DPV) or differential pulse polarography (DPP) is one of the electrochemical techniques that measures the difference between the current just before the ends of the pulse and just before the application of the pulse. It involves at least two electrodes: a working electrode which measures the current and a counter electrode through which the voltage pulses are transmitted. With regard to the different CV responses observed at the surface of the electrodes modified with compounds **1–3**, DPV was also employed to further study the electrochemical responses of these modified electrodes. Fig. 11 illustrates the various oxidation current responses of BPA determination obtained at the surface of these modified electrodes; it could be observed that the highest oxidation peak current response was obtained at the electrode modified with **3** (1.44×10^{-5} μA at 1.104 V), while the oxidation peak current at the surface of the electrode with compounds **1** and **2** are 1.64×10^{-6} μA at −0.022 V and 8.44×10^{-7} μA at 0.167 V respectively. The oxidation peak current value obtained at the electrode modified with **3** is eight times and seventeen times higher than the values obtained at the electrodes modified with compounds **1** and **2**, respectively. The synergy of the various electrochemical properties of the MOFs and TQDs that are found in the matrix of the composite could be responsible for the observation of this high oxidation peak current.[105]

4.3. Effect of concentration in the electrochemical determination of BPA using differential pulse voltammetry

Investigation on the effect of concentration in the electrochemical determination of BPA was carried out using DPV. The oxidation peak current response of various concentrations of BPA ranging from 4 nM to 16 nM is illustrated in Fig. 12, and the inset is the linear regression, showing the relationship between the BPA concentration and oxidation peak current. From Fig. 12, it can be observed that as the concentration of BPA increases, the oxidation peak current also increases linearly, which suggest an excellent relationship between the concentration of BPA and the oxidation peak current recorded at

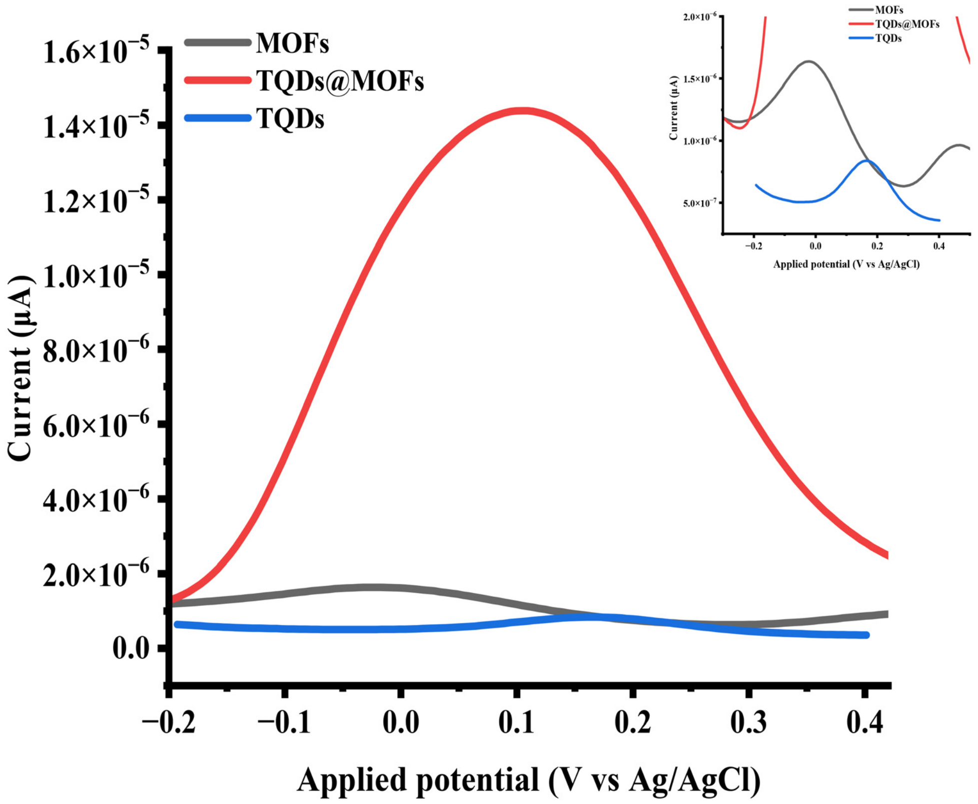

Fig. 11 Electrochemical determination of BPA on the electrodes modified with compounds **1** (MOFs), **2** (TQDs), and **3** (TQDs@MOFs) using differential pulse voltammetry (DPV).

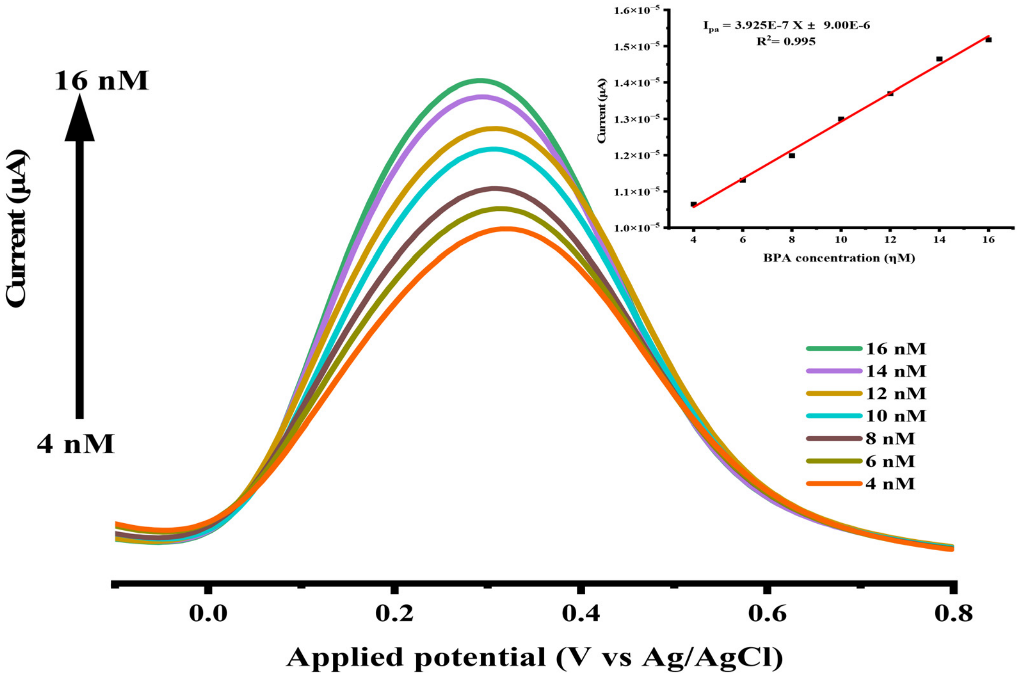

Fig. 12 Effect of the concentration increase in the electrochemical determination of BPA using DPV. The inset is the linear regression of the oxidation peak current against concentration.

the surface of the electrode modified with **3**. This outstanding oxidation peak current response could be attributed to the first-rate electrochemical conductivity, excellent sensitivity, exceptional catalytic properties, and large surface area of the electrode modified with **3**. The linear regression equation for the oxidation peak current I_{pa} is given as follows: $I_{pa} = 3.925 \times 10^{-7} \pm 9.00 \times 10^{-6}$ ($R^2 = 0.995$). Eqn (4) and (5) were used to calculate the limit of detection (LOD) and the limit of quantitation (LOQ).

$$\mathrm{LOD} = 3.3 \times (\mathrm{SD}/M) \quad (4)$$

$$\mathrm{LOQ} = 10 \times (\mathrm{SD}/M) \quad (5)$$

where SD is the standard deviation of the oxidation peak current and M is the slope of the calibration. The values obtained were as follows: LOD = 1.01 nM, and LOQ = 3.08 nM (S/N = 3). The European Union Commission (EUC) in 2004 set a specific migration limit (SML) for BPA in plastic materials to be 2.63×10^{-6} mol L^{-1}, and therefore, this electrochemical method of BPA determination using the composite of MOFs and TQDs met the requirements of the EUC.[106] The composite electrode modified with compound 3 for BPA detection ability was also examined with other previous studies (Table 6). This newly developed approach to BPA detection showed a lower detection limit and a larger linear detection range, confirming acceptable BPA detection capability.

4.4. Stability, reproducibility, and selectivity studies of the composite modified gold electrode

4.4.1. Stability. The stability of the composite modified gold electrode was investigated with 5 mM $[K_3Fe(CN)_6]$ in 0.1 M KCl at pH 7 using cyclic voltammetry. Twenty consecutive cyclic runs were performed at 150 mV s^{-1} over a potential window range of −0.2 V to 1.2 V. For all the twenty consecutive runs, a redox response was obtained with minimal or no difference in the oxidation peak current response between the first

Table 6 Comparison of the developed BPA determination method with other methods in the literature

Modified electrode	Linear range	Method used	Detection limit	Ref.
CNF/CPE	0.1 µM–60 µM	DPV	50 nM	107
$Li_4Ti_5O_{12}$/MWCNTs/GCE	0.1 µM–10 µM	DPV	78 nM	108
MIP-MWNPE	0.08 µM–100 µM	DPV	22 nM	109
PGA/MWCNTNH_2/GC	0.1 µM–10 µM	DPV	20 nM	110
SiO_2/rGO–AuNPs/GCE	0.03 µM–10 µM; 10 µM–120 µM	DPV	5 nM	111
GR-IL/GCE	0.02 µM–2 µM	LSV	8 nM	112
Ferrocenyl methyl methacrylate	4.7 to 8 nmol L^{-1}	C.V.	3.2 nmol L^{-1}	113
Rh_2O_3–rGO/GCE	0.6 µM–40 µM	Cyclic voltammetry	0.12 µM	114
$\{CuInS_2@Cu(2\text{-}MeIm)_6(BTA)_2\}$	4 nM–16 nM	DPV	1.01 nM	This work

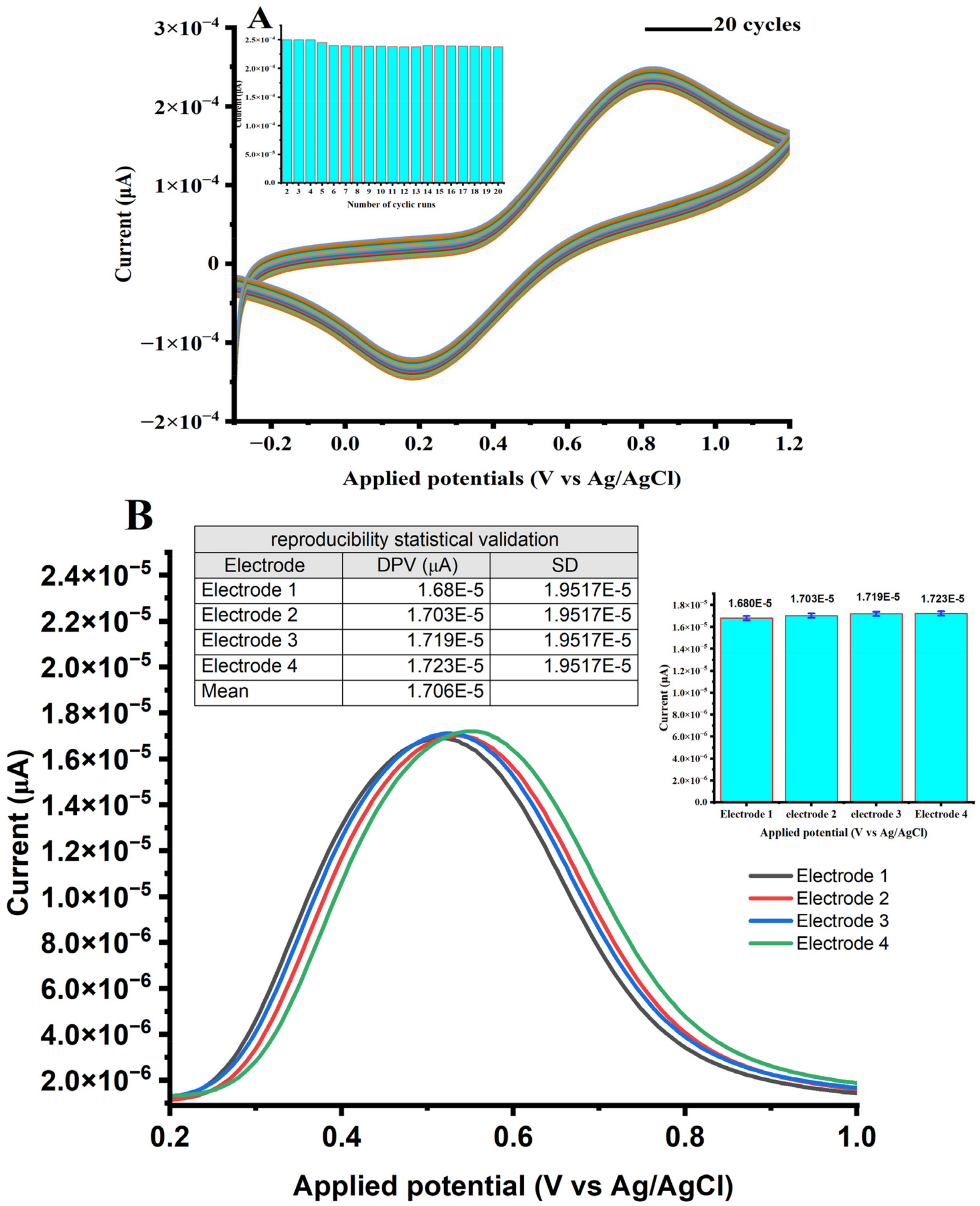

reproducibility statistical validation

Electrode	DPV (μA)	SD
Electrode 1	1.68E-5	1.9517E-5
Electrode 2	1.703E-5	1.9517E-5
Electrode 3	1.719E-5	1.9517E-5
Electrode 4	1.723E-5	1.9517E-5
Mean	1.706E-5	

Fig. 13 Stability and reproducibility of the composite electrode modified with compound **3**.

run and the last run (Fig. 13(A)). The change that is experienced in the intensity of the oxidation peak current within the twenty consecutive runs was estimated to be less than 5% (inset bar chart), signifying that the composite modified electrode is more than 95% stable. These results indicate that the composite modified electrode is reasonably stable for many more cyclic runs.

4.4.2. Reproducibility. Differential pulse voltammetry was employed to study the reproducibility of the composite modified electrode. Four (4) different electrodes were modified with the same composite under the same conditions and the oxidation peak current of 5 μM BPA in 0.1 M PBS at pH 7 at 150 mV s^{-1} over a potential window range of 0.2 V to 1 V was evaluated, and the maximum oxidation peak current response was at 0.55 V. Fig. 13B illustrates the oxidation peak current responses of the four different composite modified electrodes showing minimal or no difference in the intensity of their oxidation peak current responses (Fig. 13B inset bar chart). The calculated standard deviation of the oxidation peak current is 1.9517×10^{-7}, and the calculated mean is 1.706×10^{-5}. The relative standard deviation for the responses recorded for the four different composite modified electrodes was then calculated to be 1.14%, suggesting that they are reproducible.

4.4.3. **Selectivity.** To investigate the selectivity of the composite modified electrode, a competitive recognition study was conducted using various interfering substances in addition to BPA determination. These interfering substances are L-ascorbic acid, thiourea, and citric acid. A concentration of 5 μM BPA in 0.1 M BPS at pH 7 was prepared and 10 μM (two fold BPA concentration) of the interfering substances in 0.1 M BPS were also prepared to carry out this experiment. Cyclic voltammetry was used over the potential window range of −0.4 V to 1.1 V at a scan rate of 150 mV s^{-1} as illustrated in Fig. 14. In the inset is the bar chart of the oxidation peak current responses at the surface of the composite modified electrode against the preferred analyte and the interfering substances. It could be deduced from the result obtained that the composite modified electrode has the highest oxidation peak current response for BPA (1.111×10^{-5} μA), while its response to other interfering substances is practically negligible compared to the response for BPA, whereas no differences could be observed between the responses of interfering substances. This oxidation peak current response could be due to the electronic structure and high electrical conductivity of BPA which has an excellent electrostatic interaction with the composite at the surface of the gold electrode.[115]

4.5. Water sample assessment

For the practical application of the composite modified gold electrochemical sensor, three types of water samples were considered for the determination of BPA concentration. Tap water, treated water and untreated water samples collected from Darvill wastewater treatment plant in Pietermaritzburg, South Africa, were used for the study. These water samples were filtered using a 0.55 μm filter membrane before analysis, and a standard addition method (SAM) was used to spike the sample with BPA and DPV was employed for its determination. The concentrations of BPA in these water samples after spiking 7 mL each with 1 mL of 5 mM BPA stock solution were found to be 12.28, 23.82, and 56.47 μM, respectively. 3 mL of each spiked solution was later added to 5 mL of PBS at pH 7, and 2 mL of a known concentration of BPA varying from 4 μM to 8 μM were finally added to the above solution and the analysis was performed (Table 7). The results obtained from our study show that the percentage recovery varies from 96.46% to 101.70% and the relative standard deviation (RSD) following 5 parallel readings was observed in the range of 3.22% to 5.01%, which are very modest compared to those of the existing compounds used for BPA detection in real water samples.[115–117] The practical application in real water samples was ascertained by the response obtained at the surface of the composite modified electrode. The values of relative standard deviation, which are less than 6% (practically negligible), demonstrate that the recovery responses are satisfactory and acceptable. The drop dry method of fabrication of this electrochemical sensor offers high scalability because of its ability to expand and adapt its use across multiple sites (three different water samples) or larger monitoring systems without compromising performance. Mass production techniques like screen printing could be used for large-scale fabrication to allow multiple data collection from multiple sources. Under controlled conditions,

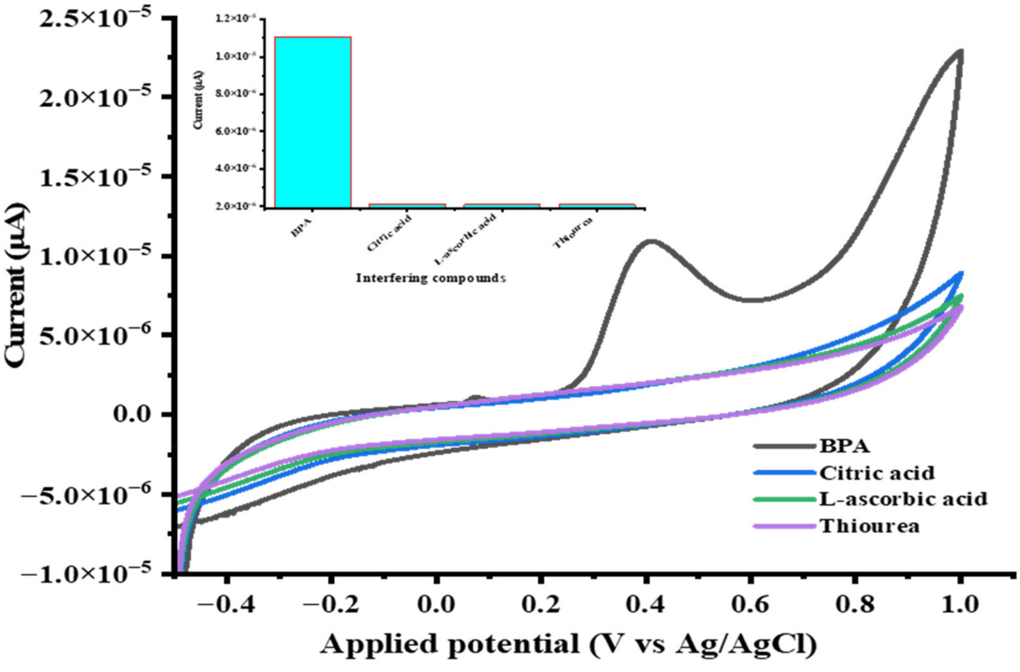

Fig. 14 Selectivity of the composite electrode modified with compound **3**.

Table 7 BPA determination in different water samples (n = 5)

Water samples	BPA concentration (μM)	Added concentration (μM)	Found (μM)	% Recovery	RSD (%)
Tap water	12.28	4	16.034	98.49	3.17
		6	18.014	98.55	4.00
		8	20.239	99.80	4.88
Treated water	23.82	4	26.835	96.46	4.00
		6	28.967	97.14	3.91
		8	31.234	98.16	4.81
Untreated water	56.47	4	58.734	97.13	3.22
		6	61.982	99.22	4.77
		8	65.565	101.70	5.06

this electrochemical sensor produced consistent results across different tests and locations for the chosen water samples, which proved their reproducibility. The cheap fabrication, deployment cost, easy maintenance and long lifespan and stability are evidence of cost-effectiveness.

5. Conclusion

Electrochemical sensors of metal–organic frameworks, ternary quantum dots and their composite were successfully fabricated using copper(II) metal–organic frameworks (MOFs), ternary quantum dots (TQDs), and their composite (TQDs@MOFs). The copper(II) complex crystallized as a centrosymmetric dimer with a pentagonal chair like conformation at the centre of symmetry in which the copper(II) ion has a distorted square pyramidal geometry. The sensor was characterized using FTIR which confirmed the presence of various functional groups in the compounds, UV-Vis which confirmed the expected electronic transitions, and SEM and TEM which revealed the morphology, inner structure and particle sizes of the compounds. A comparative study of the electrochemical oxidation peak current responses of the fabricated sensors reveals that the composite modified sensor shows the highest oxidation peak current response, and better and faster electron transfer between the preferred analyte (BPA) and the composite at the surface of the modified electrode. Under optimal conditions, the stability, reproducibility, and selectivity of the composite modified electrode were ascertained, and good electroactivity, a wide linear detection range, a low limit of detection and quantitation and a high recovery rate of BPA were also established. This excellent performance could be attributed to the electrochemical conductive properties, synergistic effect, high surface area, and intermolecular interactions between the metal–organic frameworks and ternary quantum dots that made up the composite.

Author contributions

Peter A. Ajibade: supervision, funding acquisition, project administration, conceptualization, methodology, and writing – review and editing. Solomon O. Oloyede: investigation, data curation, formal analysis, writing – original draft and visualization.

Conflicts of interest

There authors declare no conflicts of interest.

Data availability

CCDC 2345368 contains the supplementary crystallographic data for this paper.†

All supporting data for this study are presented in the ESI.†

Acknowledgements

This study was financially supported by the National Research Foundation, South Africa, through competitive support for the rated researcher, grant number CPRR23042396404.

References

1 V. Guarnotta, R. Amodei, F. Frasca, A. Aversa and C. Giordano, *Int. J. Mol. Sci.*, 2022, **23**, 5710.
2 L. Xitong, W. Jinquan, Y. Wang, Y. Zhicheng, C. Haiyuan and S. Ding, *Appl. Catal., B*, 2020, **265**, 18591.
3 K. K. Teddy, A. A. C. Martie, K. Ilunga, M. N.-J. Veronica and N. B. M. Maggy, *J. Environ. Manage.*, 2021, **277**, 111485.
4 F. Anwer, S. Chaurasia and A. Khan, *Rev. Environ. Health*, 2016, **31**(4), 415–433.
5 H. B. Patisaul, *Reproduction*, 2021, **162**(5), 111–130.
6 S. Vannuccini, V. L. Clifton, I. S. Fraser, H. S. Taylor, H. Critchley, L. C. Giudice and F. Petraglia, *Hum. Reprod. Update*, 2016, **22**(1), 104–115.
7 J. E. Schjenken, E. S. Green, T. S. Overduin, C. Y. Mah, D. L. Russell and S. A. Robertson, *Front. Endocrinol.*, 2021, **12**, 607539.
8 B. Predieri, L. Iughetti, S. Bernasconi and M. E. Street, *Int. J. Mol. Sci.*, 2022, **23**, 11899.
9 A. Alengebawy, S. T. Abdelkhalek, S. R. Qureshi and M. Q. Wang, *Toxics*, 2021, **9**, 42.

10 Y. Combarnous and T. M. D. Nguyen, *Toxics*, 2019, **7**(1), 5–12.
11 E. Chmelíková, M. Sedmíková, M. Ješeta and D. Němeček, *Med. J. Cell Biol.*, 2019, **6**(4), 135–139.
12 O. E. Omoike, R. P. Pack, H. M. Mamudu, Y. Liu and L. Wang, *Environ. Res.*, 2021, **196**, 110329.
13 B. Yilmaz, H. Terekeci and S. Sandal, *Rev. Endocr. Metab. Disord.*, 2020, **21**, 127–147.
14 I. A. Charitos, S. Topi, R. Gagliano-Candela, E. De Nitto, L. Polimeno, M. Montagnani and L. Santacroce, *Endocr., Metab. Immune Disord.: Drug Targets*, 2022, **22**(7), 716–727.
15 J. Chanemougavally, B. Thotakura, K. M. Shruthy and K. Prabhu, *Ann. Rom. Soc. Cell Biol.*, 2021, **25**(6), 10733–10741.
16 T. Ayon, S. Ranjna, A. Palanisamy, R. Reshmy, M. Aravin, S. Raveendran, B. Parameswaran, K. Yogesh, K. K. Deepa and J. S. Sang, *J. Hazard. Mater.*, 2022, **423**, 127097.
17 I. Altuwair, *Eng. Technol. Open Access*, 2018, **1**(3), 1–10.
18 J. N. Hahladakis, E. Iacovidou and S. Gerassimidou, *Environ. Toxicol. Chem.*, 2022, **19**(1), 45–46.
19 M. Thoene, L. Rytel, N. Nowicka and J. Wojtkiewicz, *Toxicol. Res.*, 2018, **7**(3), 371–380.
20 M. S. Bhuyan, *Front. Environ. Sci.*, 2022, **10**, 827289.
21 G. Hayes, M. Laurel, D. MacKinnon, T. Zhao, H. A. Houck and C. R. Becer, *Chem. Rev.*, 2023, **123**(5), 2609–2734.
22 M. Kumar, D. K. Sarma, S. Shubham, M. Kumawat, V. Verma, A. Prakash and R. Tiwari, *Front. Public Health*, 2020, **8**, 1–12.
23 R. Naomi, M. D. Yazid, H. Bahari, Y. Y. Keong, R. Rajandram, H. Embong, S. H. Teoh, S. Halim and F. Othman, *Int. J. Mol. Sci.*, 2022, **23**, 2969.
24 H. M. Sardoo, S. Sepahi, A. G. Azam, H. Askarpour, T. P. Johnston and A. Sahebkar, *Int. J. Environ. Health Res.*, 2025, **35**(5), 1314–1353.
25 Y. Cheng, H. Wang, Y. Zhuo, D. Song, C. Li, A. Zhu and F. Long, *Biosens. Bioelectron.*, 2022, **199**, 113863.
26 B. Gworek, M. Kijeńska and J. Wrzosek, *Water, Air, Soil Pollut.*, 2021, **232**, 145.
27 W. Chenhuan, L. Min, C. Xiaocui, W. Qianqian, L. Shuofeng, L. Weihua, H. Lin, W. Qiuhua and S. Xiaodong, *Talanta*, 2024, **266**(2), 125142.
28 A. Mishra, D. Goel and S. Shankar, *Environ. Monit. Assess.*, 2023, **195**, 1352.
29 L. Yanlin, W. Yiwen, M. Lanrui, F. Ruijie, L. Haoran, C. Yongliang, Z. Qiyang, Z. Yaohai, J. Bining and H. Yue, *Int. J. Biol. Macromol.*, 2022, **222**(2), 2661–2669.
30 X. Wang, R. Nag, N. P. Brunton, M. A. B. Siddique, S. M. Harrison, F. J. Monahan and E. Cummins, *Environ. Res.*, 2022, **213**, 113734.
31 N. R. Maddela, D. Kakarla, K. Venkateswarlu and M. Megharaj, *J. Environ. Manag.*, 2023, **348**, 119364.
32 N. Kataria, D. Bhushan, R. Gupta, S. Rajendran, M. Y. M. Teo and K. S. Khoo, *Environ. Pollut.*, 2022, **315**, 120319.
33 M. Dalamaga, D. Kounatidis, D. Tsilingiris, N. G. Vallianou, I. Karampela, S. Psallida and A. G. Papavassiliou, *Int. J. Mol. Sci.*, 2024, **25**, 675.
34 E. S. Gruber, V. Stadlbauer and V. Pichler, *Expos. Health*, 2023, **15**, 33–51.
35 J. D. Moreno, A. Mora, P. C. Avilés and J. Mahlknecht, *Environ. Int.*, 2022, **170**, 107550.
36 I. Cimmino, F. Fiory, G. Perruolo, C. Miele, F. Beguinot, P. Formisano and F. Oriente, *Int. J. Mol. Sci.*, 2020, **21**, 5761.
37 A. Tarafdar, R. Sirohi, P. A. Balakumaran, R. Reshmy, A. Madhavan, R. Sindhu, P. Binod, Y. Kumar, D. Kumar and S. J. Sim, *J. Hazard. Mater.*, 2022, **423**, 127097.
38 N. Nasrollahi, V. Vatanpour and A. Khataee, *Sci. Total Environ.*, 2022, **838**(1), 156010.
39 L. G. A. Barboza, S. C. Cunha, C. Monteiro, J. O. Fernandes and L. Guilhermino, *J. Hazard. Mater.*, 2020, **393**, 122419.
40 J. Rajendran, T. S. Kannan, L. S. Dhanasekaran, P. Murugan, R. Atchudan, Z. A. Alothman, M. Ouladsmane and A. K. Sundramoorthy, *Chemosphere*, 2022, **287**(2), 132106.
41 S. Campuzano, M. Pedrero, P. Yáñez-Sedeño and J. M. Pingarrón, *Sens. Actuators, B*, 2021, **345**, 130349.
42 R. Petrucci, M. Bortolami, P. D. Matteo and A. Curulli, *Nanomaterials*, 2022, **12**(6), 959.
43 F. M. Fartas, A. Jaafar, N. A. Yusof, Y. Sulaiman, M. I. Saiman and M. H. M. Zaid, *Curr. Anal. Chem.*, 2020, **16**(5), 570–579.
44 T. Xiao, J. Huang, D. Wang, T. Meng and X. Yang, *Talanta*, 2020, **206**, 120210.
45 P. Gallay, M. M. López, S. Bollo and G. Rivas, *Micromachines*, 2022, **13**, 1978.
46 A. Thamilselvan, V. Rajagopal and V. Suryanarayanan, *J. Alloys Compd.*, 2019, **786**, 698–706.
47 N. Baig and T. A. Saleh, *Microchim. Acta*, 2018, **185**, 283.
48 A. U. Alam and M. J. Deen, *Anal. Chem.*, 2020, **92**(7), 5532–5539.
49 S. K. Elsaidi, M. H. Mohamed, D. Banerjee and P. K. Thallapally, *Coord. Chem. Rev.*, 2018, **358**, 125–152.
50 Y. Wang, L. Feng, W. Fan, K.-Y. Wang, X. Wang, X. Wang, K. Zhang, X. Zhang, F. Dai, D. Sun and H.-C. Zhou, *J. Am. Chem. Soc.*, 2019, **141**(17), 6967–6975.
51 X. Liu, L. Zhang and J. Wang, *J. Materiomics*, 2021, **7**(3), 440–459.
52 G. Chakraborty, I.-H. Park, R. Medishetty and J. J. Vittal, *Chem. Rev.*, 2021, **121**(7), 3751–3891.
53 O. A. Aladesuyi, T. C. Lebepe, R. Maluleke and O. S. Oluwafemi, *Nanotechnol. Rev.*, 2022, **11**(1), 2304–2319.
54 X. Lin, C. Liu, J. Wang, S. Yang, J. Shi and Y. Hong, *Separ. Purif. Technol.*, 2019, **226**, 117–127.
55 W. M. Girma, M. Z. Fahmi, A. Permadi, M. A. Abate and J.-Y. Chang, *J. Mater. Chem. B*, 2017, **5**, 6193–6216.
56 J. Ma, K. Kang, Y. Zhang, Q. Yi and Z. Gu, *ACS Appl. Mater. Interfaces*, 2018, **10**(50), 43923–43935.
57 Y. Yu, L. Mei, Y. Shi, X. Zhang, K. Cheng, F. Cao, L. Zhang, J. Xu, X. Li and Z. Xu, *J. Mater. Chem. B*, 2020, **8**, 1371–1138.

58 K. Dewangan, T. Kant and K. Shrivas, *Nanobiotechnol. Plant Prot.*, 2022, 751–774.

59 R. D. Huelsmann, C. Will and E. Carasek, *J. Sep. Sci.*, 2021, **44**(6), 1148–1173.

60 F. Gagliani, T. Di Giulio, M. I. Asif, C. Malitesta and E. Mazzotta, *Biosensors*, 2024, **14**(7), 358.

61 L. Wenbo, S. Yafang, P. Hebing and M. Zunli, *J. Ind. Eng. Chem.*, 2023, **128**(25), 17–54.

62 O. V. Dolomanov, L. J. Bourhis, R. J. Gildea, J. A. K. Howard and H. Puschmann, *J. Appl. Crystallogr.*, 2009, **42**, 339–341.

63 G. M. Sheldrick, *Acta Crystallogr., Sect. A: Found. Adv.*, 2015, **71**, 3–8.

64 G. M. Sheldrick, *Acta Crystallogr., Sect. C: Struct. Chem.*, 2015, **71**, 3–8.

65 R. Muñoz, E. M. Santos, C. A. Galan-Vidal, J. M. Miranda, A. Lopez-Santamarina and J. A. Rodriguez, *Molecules*, 2021, **26**(9), 2764.

66 N. S. Alsaiari, H. Osman, A. Amari and M. A. Tahoon, *Magnetochemistry*, 2022, **8**, 133.

67 A. C. Tella, N. J. Shamle, J. A. Obaleye, A. C. Whitwood, S. A. Bourne and P. A. Ajibade, *J. Mol. Struct.*, 2020, **1209**, 127925.

68 Y. G. Chung, E. Haldoupis, B. J. Bucior, M. Haranczyk, S. Lee, H. Zhang, K. D. Vogiatzis, M. Milisavljevic, S. Ling, J. S. Camp, B. Slater, J. I. Siepmann, D. S. Sholl and R. Q. Snurr, *J. Chem. Eng. Data*, 2019, **64**(12), 5985–5998.

69 A. K. Patel, R. N. Jadeja and R. J. Butcher, *J. Indian Chem. Soc.*, 2021, **98**(11), 100182.

70 M. Bashir, A. A. Dar and I. Yousuf, *ACS Omega*, 2023, **8**(3), 3026–3042.

71 W. S. Mohamed and A. M. Abu-Dief, *Ceram. Int.*, 2020, **46**(10), 16196–16209.

72 Y. Cui, J. Zhang, H. He and G. Qian, *Chem. Soc. Rev.*, 2018, **47**, 5740–5785.

73 R. Atchudan, T. N. J. I. Edison, D. Chakradhar, S. Perumal, J. J. Shim and Y. R. Lee, *Sens. Actuators, B*, 2017, **246**, 497–509.

74 P. F. Andrade, G. Nakazato and N. Durán, *J. Phys.: Conf. Ser.*, 2017, **838**, 012028.

75 Y. Hu, X. Geng, L. Zhang, Z. Huang, J. Ge and Z. Li, *Sci. Rep.*, 2017, **7**, 1–9.

76 N. V. Reis, A. C. Deacy, G. Rosetto, C. B. Durr and C. K. Williams, *Chem. – Eur. J.*, 2022, **28**(14), 1–12.

77 M. Richezzi, S. Signorella, C. Palopoli, N. Pellegri, C. Hureau and S. R. Signorella, *Inorganics*, 2023, **11**, 359.

78 D. Dutta, P. Sharma, A. Frontera, A. Gogoi, A. K. Verma, D. Dutta, B. Sarma and M. K. Bhattacharyya, *New J. Chem.*, 2020, **44**, 20021–20038.

79 N. Ahn, C. Livache, V. Pinchetti and V. I. Klimov, *Chem. Rev.*, 2023, **123**(13), 8251–8296.

80 D. Zhang, Z. Wu and X. Zong, *Sens. Actuators, B*, 2019, **288**(1), 232–242.

81 F. Al-dolaimy, U. S. Altimari, A. S. Abdulwahid and A. H. R. Abbas, *J. Inorg. Organomet. Polym. Mater.*, 2023, **34**(59A), 1–11.

82 M. I. Rahman, H. M. Khan, M. N. Ashiq, M. U. Islam, S. A. Buzdar, I. Sadiq, S. Honey, Z. Batool, R. Sheikh, M. Zahid, M. A. Assiri, M. Imran and T. Alshahrani, *RSC Adv.*, 2023, **13**, 14461–14471.

83 S. Gao, Y. Sui, F. Wei, J. Qi, Q. Meng and Y. He, *J. Mater. Sci.: Mater. Electron.*, 2018, **29**, 2477–2483.

84 S. Kashiwaya, C. Aymonier, J. Majimel, C. Olivier, A. Klein, W. Jaegermann and T. Toupance, *New J. Chem.*, 2018, **42**, 18649–18658.

85 P. Makuła, M. Pacia and W. Macyk, *Phys. Chem. Lett.*, 2018, **9**(23), 6814–6817.

86 M. Treger, A. Hannebauer, A. Schaate, J. L. Budde, P. Behrens and A. M. Schneider, *Phys. Chem. Chem. Phys.*, 2023, **25**, 6333–6341.

87 F. H. Isikgor, S. T. Zhumagali and L. V. Merino, *Nat. Rev. Mater.*, 2023, **8**, 89–108.

88 K. W. Cho, S.-H. Sunwoo, Y. J. Hong, J. H. Koo, J. H. Kim, S. Baik, T. Hyeon and D. H. Kim, *Chem. Rev.*, 2022, **122**(5), 5068–5143.

89 X. Chen, X. Zhang, X. Xiao, Z. Wang and J. Zhao, *Angew. Chem., Int. Ed.*, 2023, **62**(16), e202216010.

90 C. Ximin, R. Qifeng, Z. Xiaolu, X. Xinyue, H. Jingtian, F. Runfang, L. Yang, W. Jianfang and X. Hongxing, *Chem. Rev.*, 2023, **123**(11), 6891–6952.

91 N. D. Adamopoulos, N. G. Tsierkezos, A. Ntziouni, F. Zhang, M. Terrones and K. V. Kordatos, *Carbon*, 2023, **213**, 118178.

92 R. Jarošová, K. Bhardwaj and G. M. Swain, *J. Electroanal. Chem.*, 2020, **875**, 114744.

93 L. Yana, X. Yana, H. Lia, X. Zhanga, M. Wanga, S. Fub, G. Zhangb, C. Qiana, H. Yanga, J. Hana and F. Xiao, *Microchem. J.*, 2020, **157**, 105016.

94 E. B. Bahadır and M. K. Sezgintürk, A review on impedimetric biosensors, *Artif. Cells, Nanomed. Biotechnol.*, 2016, **44**, 248–262.

95 S. Wang, J. Zhang, O. Gharbi, V. Vivier, M. Gao and M. E. Orazem, Electrochemical impedance spectroscopy, *Nat. Rev. Methods Primers*, 2021, **1**(41), 1–58.

96 G. Saldaña, J. I. S. Martín, I. Zamora, F. J. Asensio and O. Oñederra, *Energies*, 2019, **12**(14), 2750.

97 H. S. Magar, R. Y. A. Hassan and A. Mulchandani, *Sensors*, 2021, **21**, 6578.

98 I. Navitski, A. Ramanaviciute, S. Ramanavicius, M. Pogorielov and A. Amanavicius, *Nanomaterials*, 2024, **14**, 447.

99 R. Ahmed, M. Nargis and A. B. Ihsan, *Mater. Res. Found.*, 2023, **141**, 246–269.

100 D. Yun, V. de Serrano and R. A. Ghiladi, *J. Inorg. Biochem.*, 2023, **238**, 112020.

101 M. Shirani, A. Aslani, S. Sepahi, E. Parandi, A. Motamedi, E. Jahanmard, H. R. Nodeh and B. Akbari-adergani, *Anal. Methods*, 2022, **14**, 2623–2630.

102 A. U. Alam and M. J. Deen, *Anal. Chem.*, 2020, **92**(7), 5532–5539.

103 Y. Yang, H. Zhang, C. Huang and N. Jia, *Sens. Actuators, B*, 2016, **235**, 408–413.

104 C. Orha, C. Bandas, C. Lazau and F. Manea, *Water*, 2022, **14**(5), 821.

105 N. Ghaffari, K. Pokpas, E. Iwuoha and N. Jahed, *Anal. Lett.*, 2024, **57**(6), 1008–1025.

106 T. Beduk, A. A. Lahcen, N. Tashkandi and K. N. Salama, *Sens. Actuators, B*, 2020, **314**, 128026.

107 J. Sun, Y. Liu, S. Lv, Z. Huang, L. Cui and T. Wu, *Electroanalysis*, 2016, **28**(3), 439–444.

108 A. U. Alam and M. J. Deen, *Anal. Chem.*, 2020, **92**(7), 5532–5539.

109 Z. Chen, W. Wei, X. Liu and B. J. Ni, *Water Res.*, 2022, **221**, 118846.

110 F. Shanshan, Z. Yuan, Y. Zhang, Z. Mingjuan, Z. Yuanyuan, L. Qiao, Y. Nian, S. Kexin, L. Mengsi and W. Dongbo, *Microchem. J.*, 2021, **171**, 106776.

111 O. Moradi, *Food Chem. Toxicol.*, 2022, **165**, 113074.

112 Z. Yuyao, L. Yajie and T. Salma, *J. Water Process. Eng.*, 2024, **61**, 105286.

113 L. J. Ling, J. P. Xu, Y. H. Deng, Q. Peng, J. H. Chen, Y. San He and Y. J. Nie, *Anal. Methods*, 2018, **10**, 2722–2730.

114 R. Shi, X. Yuan, A. Liu, M. Xu and Z. Zhao, *Appl. Sci.*, 2018, **8**, 2535.

115 F. Yang and F. Zhao, *J. Hazard. Mater.*, 2023, **443**, 130214.

116 X. Lei, Z. Deng, Y. Zeng, S. Huang, Y. Yang, H. Wang, L. Guo and L. Li, *Sens. Actuators, B*, 2021, **339**, 129885.

117 J. Zoua, G.-Q. Zhaoa, J. Tengb, Q. Liua, X.-Y. Jianga, F.-P. Jiaoa and J.-G. Yu, *Microchem. J.*, 2019, **145**, 693–702.